

Multisensor Coupled Spectral Unmixing for Time-Series Analysis

Naoto Yokoya, *Member, IEEE*, Xiao Xiang Zhu, *Senior Member, IEEE*, and Antonio Plaza, *Fellow, IEEE*

Abstract—We present a new framework, called *multisensor coupled spectral unmixing* (MuCSUn), that solves unmixing problems involving a set of multisensor time-series spectral images in order to understand dynamic changes of the surface at a subpixel scale. The proposed methodology couples multiple unmixing problems based on regularization on graphs between the time-series data to obtain robust and stable unmixing solutions beyond data modalities due to different sensor characteristics and the effects of nonoptimal atmospheric correction. Atmospheric normalization and cross calibration of spectral response functions are integrated into the framework as a preprocessing step. The proposed methodology is quantitatively validated using a synthetic data set that includes seasonal and trend changes on the surface and the residuals of nonoptimal atmospheric correction. The experiments on the synthetic data set clearly demonstrate the efficacy of MuCSUn and the importance of the preprocessing step. We further apply our methodology to a real time-series data set composed of 11 Hyperion and 22 Landsat-8 images taken over Fukushima, Japan, from 2011 to 2015. The proposed methodology successfully obtains robust and stable unmixing results and clearly visualizes class-specific changes at a subpixel scale in the considered study area.

Index Terms—Change detection, coupled spectral unmixing, multisensor data fusion, time-series analysis.

NOMENCLATURE

B	Number of bands.
B_0	Maximum number of bands.
P	Number of pixels.
M	Number of endmembers.
N	Number of time-series images.
K	Number of neighbors.
\mathbf{Y}	Spectral data matrix $B \times P$.
\mathbf{A}	Endmember matrix $B \times M$.
\mathbf{X}	Abundance matrix $P \times M$.

\mathbf{N}	Residual matrix $B \times P$.
\mathbf{R}	Relative spectral response function (SRF) $B \times B_0$.
\mathbf{c}_0	Residual offset vector $B \times 1$.
\mathbf{c}_1	Residual gain vector $B \times 1$.
\mathbf{W}	Weighting matrix on graph $P \times P$.
\mathbf{G}	Adjacency matrix $(K + 1) \times (K + 1)$.

I. INTRODUCTION

ASYNERGETIC use of hyperspectral (HS) and multispectral (MS) images is important for upcoming spaceborne HS imaging projects [1]–[5]. Spaceborne HS imaging is capable of monitoring and interpreting detailed dynamic processes of the surface on a global scale; however, revisit time is limited compared with MS imaging satellites. For example, the environmental mapping and analysis program (EnMAP) [1], which will record more than 240 spectral bands at 0.4–2.5 μm at a ground sampling distance of 30 m, has a 27-day revisit cycle (off-nadir four days). In contrast, recent MS satellites have higher revisit times, e.g., Landsat-8 has a 16-day revisit cycle and Sentinel-2 will exhibit a 5-day revisit cycle with a constellation of two operational satellites (10 days with one satellite) [6], [7]. Improved understanding of the dynamics on the surface is expected by synergistically analyzing a set of time-series spaceborne HS and MS images.

In the last decade, research on the analysis of time-series HS images has focused on pixel-level change detection. One of the first examples of change detection using bitemporal HS images is presented in [8]. Linear-transform-based methods have been investigated as a major unsupervised approach. Change vector analysis [12], which was originally proposed for analyzing MS images and is now widely used in various applications, has been extended to unsupervised detection of multiple changes using multitemporal HS images [13], [14]. Target or anomaly detection techniques have been naturally applied to change detection using multiple HS images [15]–[17]. Classification has also been demonstrated to be a powerful supervised approach to obtaining changes from multitemporal and multi-source spectral data [18].

In recent years, research on time-series HS unmixing has been receiving particular attention due to its ability to understand class-specific changes at a subpixel level [19]–[29]. One of the first examples of time-series HS unmixing is presented in [19]. Several publications on multitemporal spectral unmixing have shown its efficacy in a wide range of applications [19]–[23]. Recent advances focused on applying spectral-library-based unmixing methods to multitemporal unmixing problems [22], [26]. A data-driven (unsupervised) approach has also been proposed in [27]–[29].

Manuscript received March 4, 2016; revised October 5, 2016; accepted January 15, 2017. Date of publication February 22, 2017; date of current version March 17, 2017. This work was supported in part by the Japan Society for the Promotion of Science through KAKENHI under Grant 15K20955, in part by Alexander von Humboldt Fellowship for post-doctoral researchers, and in part by the Helmholtz Young Investigators Group “SiPEO” under Grant VH-NG-1018.

N. Yokoya is with the Department of Advanced Interdisciplinary Studies, University of Tokyo, Tokyo 153-8904, Japan, and also with the Remote Sensing Technology Institute, German Aerospace Center, 82234 Wessling, Germany, and also with Signal Processing in Earth Observation, Technical University of Munich, 80333 Munich, Germany (e-mail: yokoya@sal.rcast.u-tokyo.ac.jp).

X. X. Zhu is with the Remote Sensing Technology Institute, German Aerospace Center, 82234 Wessling, Germany, and also with Signal Processing in Earth Observation, Technical University of Munich, 80333 Munich, Germany (e-mail: xiao.zhu@dlr.de).

A. Plaza is with the Hyperspectral Computing Laboratory, Department of Technology of Computers and Communications, University of Extremadura, E-10003 Cáceres, Spain (e-mail: aplaza@unex.es).

Color versions of one or more of the figures in this paper are available online at <http://ieeexplore.ieee.org>.

Digital Object Identifier 10.1109/TGRS.2017.2655115

To the best of the authors' knowledge, time-series spectral unmixing has been scarcely investigated from the viewpoint of synergistically exploiting HS and MS images. To tackle multisensor time-series spectral unmixing, determining how to use HS and MS images in a complementary fashion is a challenging issue: there is no standard framework available. In addition, most of the previous studies on time-series HS unmixing do not take into account possible data mismatches due to nonoptimal atmospheric correction, even though it always appears in time-series spectral data [30]–[32].

This paper proposes a novel framework, called *multisensor coupled spectral unmixing* (MuCSUn), for time-series analysis. Our goal is to understand dynamic changes on the surface at a subpixel scale from multisensor time-series data, beyond data modalities, due to different sensor characteristics and the effects of nonoptimal atmospheric correction. A single spectral unmixing problem is solved jointly with those related to other images that have similar surface conditions to obtain a robust, stable, and accurate solution. Regularization on graphs between neighborhood images is used to couple multiple unmixing problems. Our technical contribution is twofold: 1) we propose a MuCSUn algorithm based on regularization on graphs between multisensor and multitemporal spectral images and 2) we introduce cross-calibration methods for estimating relative SRFs and residual gains and offsets due to nonoptimal atmospheric correction and integrate them into the MuCSUn framework.

The remainder of this paper is organized as follows. Section II introduces our methodology. The experimental results on synthetic and real data sets are presented in Sections III and IV, respectively. Section V concludes this paper with some remarks and hints at plausible future research lines.

II. METHODOLOGY

We first provide an overview of the linear spectral unmixing chain that forms the basis for our methodology. Next, we formulate an optimization problem for MuCSUn based on graphs between multisensor time-series images and derive an algorithm using the augmented Lagrangian method. Finally, we introduce cross-calibration methods for estimating relative SRFs and residual gains and offsets due to nonoptimal atmospheric correction.

A. Linear Spectral Unmixing

A linear spectral mixture model is commonly used for unmixing problems owing to its physical effectiveness and mathematical simplicity. The spectrum at each pixel is assumed to be a linear combination of several endmember spectra. Therefore, an HS image $\mathbf{Y} \in \mathbb{R}^{B \times P}$, with B bands and P pixels, is formulated as

$$\mathbf{Y} = \mathbf{A}\mathbf{X}^T + \mathbf{N} \quad (1)$$

where $\mathbf{A} \in \mathbb{R}^{B \times M}$ is the spectral signature matrix, with M being the number of endmembers, $\mathbf{X} \in \mathbb{R}^{P \times M}$ is the abundance matrix, $\mathbf{N} \in \mathbb{R}^{B \times P}$ is the residual, and the operator $()^T$ denotes the transposition operation. Assuming that the residual is approximated as zero-mean white Gaussian noise, a spectral

unmixing problem can be generally formulated as

$$\begin{aligned} \min_{\mathbf{A}, \mathbf{X}} \quad & \|\mathbf{Y} - \mathbf{A}\mathbf{X}^T\|_F^2 + f(\mathbf{A}, \mathbf{X}) \\ \text{s.t.} \quad & \mathbf{A} \succeq \mathbf{0}, \mathbf{X} \succeq \mathbf{0}, \mathbf{X}\mathbf{1}_M = \mathbf{1}_P \end{aligned} \quad (2)$$

where $\|\cdot\|_F$ denotes the Frobenius norm and $f(\mathbf{A}, \mathbf{X})$ is a regularization term. $\mathbf{1}_M$ and $\mathbf{1}_P$ are column vectors with all elements being equal to one; the subscripts denote the number of elements. The abundance nonnegativity constraint ($\mathbf{X} \succeq \mathbf{0}$) and the abundance sum-to-one constraint ($\mathbf{X}\mathbf{1}_M = \mathbf{1}_P$) are widely used in the literature [33]. In cases when spectral variability explained by scaling is considered, it is proper to assume that the abundance fractions sum to less than one ($\mathbf{X}\mathbf{1}_M \leq \mathbf{1}_P$). It can be also implemented with the sum-to-one constraint by adding a shade endmember. Researchers have studied many models and algorithms based on geometrical, statistical, and sparse regression-based approaches in search of robust, stable, tractable, and accurate unmixing [34].

When the spectral signature matrix \mathbf{A} is available, the main task of spectral unmixing is to determine the abundances \mathbf{X} . Here we suppose that the spectral signature matrix is obtained either from a spectral library or from the data itself, satisfying the condition $M \leq B$. When $f(\mathbf{A}, \mathbf{X}) = 0$, the abundances can be obtained by solving constrained least-squares (CLS) problems for all pixels via quadratic programming [35].

Since the number of endmembers at each pixel is usually very limited, sparsity of abundances can be also used as an additional constraint: $\|\mathbf{X}^j\|_0 \leq K, j = 1, \dots, P$, where \mathbf{X}^j denotes the j th row vector of \mathbf{X} . Combinatorial optimization methods are useful for solving this problem and commonly adopted in various applications [36]. In recent years, sparse regression methods have attracted particular attention due to the concurrent theoretical development of compressed sensing [37]–[41]. These approaches can solve the problem, even if it is underdetermined owing to the presence of a large number of spectral signatures in \mathbf{A} ($M > B$).

Data-driven endmember extraction methods have been widely investigated as a means of handling cases where the spectral signature matrix (\mathbf{A}) is unknown. Geometrical-based approaches such as pure pixel index [42], N-FINDR [43], and vertex component analysis (VCA) [44] are popular, with their assumption that pure pixels of all endmembers are included in the data. Minimum volume based algorithms were developed to tackle the problem without the pure pixel assumption [45]. After determining \mathbf{A} , we can obtain \mathbf{X} by the CLS method.

Nonnegative matrix factorization (NMF) algorithms [46], [47] have emerged as useful unmixing methods because they overcome the difficulties related to the absence of pure pixels with straightforward implementation and sufficient mathematical flexibility to consider several constraints [48]–[54]. NMF based algorithms solve (2) via alternating optimization. NMF alternately minimizes the objective function over \mathbf{A} with \mathbf{X} fixed and over \mathbf{X} with \mathbf{A} fixed with proper initialization, e.g., using the above-mentioned methods based on the pure pixel assumption. Various regularization terms have shown to be effective, for example, minimum volume regularization [48], $L_{1/2}$ sparsity regularization [52], and graph regularization [53].

In this paper, we formulate spectral unmixing of each temporal image based on (2) and adopt alternating optimization for flexibility, with conventional methods being used for initialization. The $L_{1/2}$ sparsity regularization on abundances is considered for the regularization term owing to its strong sparsity promotion even with the abundance sum-to-one constraint. The $L_{1/2}$ regularization term is defined as

$$f(\mathbf{X}) = \alpha \|\mathbf{X}\|_{1/2}^{1/2} \quad (3)$$

where $\|\mathbf{X}\|_{1/2}^{1/2} = \sum_{j,m}^{P,M} |(\mathbf{X})_{jm}|^{1/2}$ and $(\mathbf{X})_{jm}$ denotes the (j, m) th entry of the matrix \mathbf{X} . The parameter α controls the sparsity of the abundances and can be estimated based on the sparseness criterion in [55], which is defined by

$$\alpha = \frac{1}{\sqrt{B}} \sum_{i=1}^B \frac{\sqrt{P} - \|\mathbf{Y}^i\|_1 / \|\mathbf{Y}^i\|_2}{\sqrt{P-1}}. \quad (4)$$

B. Multisensor Coupled Spectral Unmixing With Graph Regularization

To tackle spectral unmixing of multisensor time-series data, we have to handle data modalities due to environmental conditions and instrumental configurations. In this paper, we take into account the effects of nonoptimal atmospheric correction and SRFs that mainly characterize the data modality. The linear spectral mixture model is thus rewritten as

$$\mathbf{Y} = \text{diag}(\mathbf{1}_B + \mathbf{c}_1) \mathbf{R} \mathbf{A} \mathbf{X}^T + \mathbf{c}_0 \mathbf{1}_P^T + \mathbf{N} \quad (5)$$

where $\mathbf{c}_1 \in \mathbb{R}^{B \times 1}$ is a vector with each element representing the residual gain for each band (an ideal value is 0), $\mathbf{R} \in \mathbb{R}^{B \times B_0}$ is the relative SRFs resampled with B_0 bands, $\mathbf{c}_0 \in \mathbb{R}^{B \times 1}$ is a vector with each element representing the residual offset for each band (an ideal value is 0), and the spectral signature matrix has B_0 bands. In cases where data-driven endmember extraction methods are used, B_0 is defined as the number of spectral bands of the highest spectral resolution among multiple spectral imagers. When we use a spectral library for the endmember spectral signatures, B_0 is defined by the spectral resolution of the library.

We first focus on estimating the spectral signatures (\mathbf{A}) and the abundances (\mathbf{X}), assuming that the residual parameters (\mathbf{c}_0 and \mathbf{c}_1) for refinement of atmospheric correction (or atmospheric normalization) and the relative SRFs (\mathbf{R}) are known but contain some errors. The estimation of (\mathbf{c}_0 , \mathbf{c}_1) and \mathbf{R} will be given in Section II-C. If we replace $\text{diag}(\mathbf{1}_B + \mathbf{c}_1)^{-1}(\mathbf{Y} - \mathbf{c}_0 \mathbf{1}_P^T)$ with \mathbf{Y} and $\mathbf{R} \mathbf{A}$ with \mathbf{A} , (5) can be simplified to the traditional linear spectral mixture model shown in (1). In other words, the traditional linear spectral mixture model assumes perfect atmospheric correction and knowledge of the SRF, although the former condition may never happen in real cases [32], particularly when we deal with multisensor time-series data. Therefore, it is important to unmix multiple spectral images on a coupled basis to achieve robustness to residuals in atmospheric correction and relative SRFs.

To this end, we introduce MuCSUn, which solves an unmixing problem of a single image jointly with those of its neighboring images (in the time-series hierarchy) by adopting

an intrinsic manifold of the time-series data set. Fig. 1 illustrates the manifold of multisensor time-series spectral data. Each sample represents a single image. Owing to changes on the surface, the multisensor time-series data set forms the manifold, where neighborhood images have similar conditions of the surface. We formulate MuCSUn as a decentralized optimization problem for multiagent systems [56], i.e., each spectral unmixing instance solves a local optimization problem based only on information concerning other spectral unmixing problems in its neighborhood.

We use regularization on local graphs to couple the multiple spectral unmixing problems. In a local graph, a target image and its neighbors, which are regarded as nodes, are connected by edges. Local graphs can be mixtures between undirected and directed graphs, depending on the difference in the spectral resolution between the two images. We use undirected graphs between images with a similar spectral resolution so that local spectral unmixing problems mutually influence each other. The accuracy of the individual spectral unmixing (ISU) problems depends highly on the spectral resolution of the data, e.g., HS imaging enables more accurate spectral unmixing than MS imaging. If the target image is an MS data set, HS neighboring images can improve the accuracy of the spectral unmixing for the target image; however, the reverse is not necessarily the case. Therefore, we also consider directed graphs, where the edges have a direction from higher spectral resolution data to lower spectral resolution data in the manifold (Fig. 1).

Let us consider $K+1$ images $\{\mathbf{Y}_k \in \mathbb{R}^{B_k \times P}\}_{k=1}^{K+1}$, i.e., a target image and its K -nearest neighbors. The numbers of spectral bands satisfy $B_1 \leq B_2 \leq \dots \leq B_{K+1}$ without loss of generality. For ISU, we adopt the $L_{1/2}$ sparsity regularization on abundances. The problem of coupled spectral unmixing can be formulated as

$$\begin{aligned} \min_{\mathbf{A}, \mathbf{X}, \mathbf{B}, \mathbf{Z}} & \frac{1}{2} \sum_{k=1}^{K+1} \|\mathbf{Y}_k - \mathbf{A}_k \mathbf{X}_k^T\|_F^2 + \alpha \sum_{k=1}^{K+1} \|\mathbf{X}_k\|_{1/2}^{1/2} \\ & + \frac{1}{2} \beta \sum_{p=1}^K \sum_{q=p+1}^{K+1} \sum_{j,l=1}^P \\ & ((\mathbf{G})_{pq} (\mathbf{G})_{qp} \|\mathbf{X}_p^j - \mathbf{X}_q^l\|_2^2 \\ & + ((\mathbf{G})_{qp} - (\mathbf{G})_{pq}) \|\mathbf{X}_p^j - \mathbf{Z}_q^l\|_2^2) (\mathbf{W}_{pq})_{jl} \\ & + \gamma \sum_{p=1}^K \sum_{q=p+1}^{K+1} \\ & ((\mathbf{G})_{pq} (\mathbf{G})_{qp} \|\mathbf{R}_{pq} \mathbf{A}_q - \mathbf{A}_p\|_F^2 \\ & + ((\mathbf{G})_{qp} - (\mathbf{G})_{pq}) \|\mathbf{R}_{pq} \mathbf{B}_q - \mathbf{A}_p\|_F^2) \end{aligned} \quad (6)$$

s.t. $\mathbf{A}_k \geq \mathbf{0}$, $\mathbf{X}_k \geq \mathbf{0}$, $\mathbf{X}_k = \mathbf{Z}_k$, $\mathbf{A}_k = \mathbf{B}_k$, $\mathbf{X}_k \mathbf{1}_M = \mathbf{1}_P$

where $\mathbf{A} = [\mathbf{A}_1^T, \dots, \mathbf{A}_{K+1}^T]^T$, $\mathbf{X} = [\mathbf{X}_1^T, \dots, \mathbf{X}_{K+1}^T]^T$, and $\mathbf{A}_k \in \mathbb{R}^{B_k \times M}$ and $\mathbf{X}_k \in \mathbb{R}^{P \times M}$ denote the spectral signature matrix and the abundance matrix of the k th data \mathbf{Y}_k , respectively. $\mathbf{B} = [\mathbf{B}_1^T, \dots, \mathbf{B}_{K+1}^T]^T$ and $\mathbf{Z} = [\mathbf{Z}_1^T, \dots, \mathbf{Z}_{K+1}^T]^T$ are auxiliary variables that are introduced to implement the directed-graph regularization. In addition to the $L_{1/2}$ sparsity constraint for each unmixing, the term with the parameter β is the graph regularization, which places the restriction such that if two spectral signatures are similar, the abundance

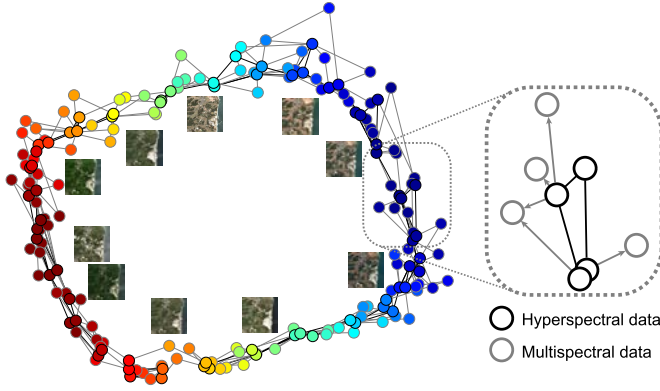


Fig. 1. Manifold of multisensor time-series spectral data.

vectors are also similar to each other. $\mathbf{W}_{pq} \in \mathbb{R}^{P_p \times P_q}$ is the weight matrix on the graph between the p th and q th data and $(\mathbf{W}_{pq})_{jl}$ represents the closeness of two points: the j th column of \mathbf{Y}_p and the l th column of \mathbf{Y}_q . Using the last penalty term with the parameter γ , we expect that the neighborhood images share similar endmember signatures. $\mathbf{R}_{pq} \in \mathbb{R}^{B_p \times B_q}$ is the relative SRF defined between the sensors that observed the p th and q th data. $\mathbf{G} \in \mathbb{R}^{(K+1) \times (K+1)}$ is the adjacency matrix that represents the local graph between $K+1$ images. $\mathbf{G}_{pq} = \mathbf{G}_{qp} = 1$ if the p th and q th images are connected by the undirected edge, whereas $\mathbf{G}_{pq} = 0$ and $\mathbf{G}_{qp} = 1$ if they are connected by the directed edge from the q th image to the p th image

The formula in (6) can be solved by alternating optimization. The alternating update rules (7)–(12), shown at the bottom of the page, are obtained by the augmented Lagrangian method. More details on deriving these update rules are given in the Appendix. $\mathbf{X}_k^{-1/2}$ denotes a matrix where each element is the reciprocal of the square root of the element in $\mathbf{X}_k > \mathbf{0}$. If any entry becomes zero in \mathbf{X}_k , a very small positive number will be added to satisfy $\mathbf{X}_k > \mathbf{0}$ [52]. Υ_k and Θ_k are the Lagrange multipliers and $\sigma > 0$ and $\rho > 0$ are the penalty parameters. $\mathbf{D}_{pq1} \in \mathbb{R}^{P_p \times P_p}$ and $\mathbf{D}_{pq2} \in \mathbb{R}^{P_q \times P_q}$ denote

diagonal matrices whose entries are row and column sums of \mathbf{W}_{pq} , respectively.

We detail how to select the K -nearest neighbors for each target image and construct the matrices \mathbf{G} and \mathbf{W} . We present two strategies for neighbors selection, namely, *sequential coupling* and *manifold-based coupling*. Sequential coupling selects temporally neighboring K images. Manifold-based coupling finds the K -nearest neighbors of a target image based on the spectral similarity measurement over the whole scene using a distance metric, such as the heat kernel, spectral angle distance (SAD), or spectral information divergence (SID). We calculate the spectral similarity between the target image and the other images on a pixel-by-pixel basis. The average of calculated similarity values is used to find the K -nearest neighbors. After finding the neighbors, the adjacency matrix \mathbf{G} is constructed based on the spectral resolution so that images with a similar spectral resolution are connected by undirected edges and directed edges are drawn from higher spectral resolution data to lower spectral resolution data.

\mathbf{W} is defined by the spectral similarity measurement using the same distance metric as the one used for neighbors selection. The choice of a distance metric depends on characteristics of multisensor time-series images. In this paper, the heat kernel is used for synthetic data in Section III, whereas the SAD is used for real data in Section IV to deal with locally variable atmospheric conditions (e.g., thin clouds). Note that the spectral similarity measurement is carried out with the lowest spectral resolution for consistency of measured values by spectrally downgrading higher spectral resolution data using the relative SRF. The simplest way to construct \mathbf{W} is to calculate the spectral similarity between only a pair of spatially corresponding pixels. In this case, $\mathbf{W}_{pq} = \mathbf{D}_{pq1} = \mathbf{D}_{pq2}$ if $P_p = P_q$ is satisfied. We use this technique to save computational costs.

Note that (7)–(12) are the update rules for solving (6) without the sum-to-one constraint. To satisfy the abundance sum-to-one constraint, the data matrix \mathbf{Y}_k and the spectral

$$(\mathbf{A}_k)_{im} \leftarrow (\mathbf{A}_k)_{im} \frac{\left(\mathbf{Y}_k \mathbf{X}_k + \gamma \left(\sum_{p=1}^{k-1} (\mathbf{G})_{pk} (\mathbf{G})_{kp} \mathbf{R}_{pk}^T \mathbf{A}_p + \sum_{q=k+1}^{K+1} ((\mathbf{G})_{kq} (\mathbf{G})_{qk} \mathbf{R}_{kq} \mathbf{A}_q + ((\mathbf{G})_{qk} - (\mathbf{G})_{kq}) \mathbf{R}_{kq} \mathbf{B}_q) \right) + \Upsilon_k \right)_{im}}{\left(\mathbf{A}_k \mathbf{X}_k^T \mathbf{X}_k + \gamma \left(\sum_{p=1}^{k-1} (\mathbf{G})_{pk} (\mathbf{G})_{kp} \mathbf{R}_{pk}^T \mathbf{R}_{pk} \mathbf{A}_k + \sum_{q=k+1}^{K+1} ((\mathbf{G})_{kq} (\mathbf{G})_{qk} + (\mathbf{G})_{qk} - (\mathbf{G})_{kq}) \mathbf{A}_k \right) \right)_{im}} \quad (7)$$

$$(\mathbf{B}_k)_{im} \leftarrow (\mathbf{B}_k)_{im} \frac{\left(\gamma \sum_{p=1}^{k-1} ((\mathbf{G})_{kp} - (\mathbf{G})_{pk}) \mathbf{R}_{pk}^T \mathbf{A}_p + \sigma \mathbf{A}_k \right)_{im}}{\left(\gamma \sum_{p=1}^{k-1} ((\mathbf{G})_{kp} - (\mathbf{G})_{pk}) \mathbf{R}_{pk}^T \mathbf{R}_{pk} \mathbf{B}_k + \Upsilon_k + \sigma \mathbf{B}_k \right)_{im}} \quad (8)$$

$$(\Upsilon_k)_{im} \leftarrow (\Upsilon_k)_{im} + \sigma (\mathbf{B}_k - \mathbf{A}_k)_{im} \quad (9)$$

$$(\mathbf{X}_k)_{jm} \leftarrow (\mathbf{X}_k)_{jm} \frac{\left(\mathbf{Y}_k^T \mathbf{A}_k + \beta \left(\sum_{p=1}^{k-1} \mathbf{G}_{pk} \mathbf{G}_{kp} \mathbf{W}_{pk}^T \mathbf{X}_p + \sum_{q=k+1}^{K+1} ((\mathbf{G})_{kq} (\mathbf{G})_{qk} \mathbf{W}_{kq} \mathbf{X}_q + ((\mathbf{G})_{qk} - (\mathbf{G})_{kq}) \mathbf{W}_{kq} \mathbf{Z}_q) \right) + \Theta_k \right)_{jm}}{\left(\mathbf{X}_k \mathbf{A}_k^T \mathbf{A}_k + \alpha \mathbf{X}_k^{-1/2} + \beta \left(\sum_{p=1}^{k-1} (\mathbf{G})_{pk} (\mathbf{G})_{kp} \mathbf{D}_{pk2} \mathbf{X}_k + \sum_{q=k+1}^{K+1} ((\mathbf{G})_{kq} (\mathbf{G})_{qk} + (\mathbf{G})_{qk} - (\mathbf{G})_{kq}) \mathbf{D}_{kq1} \mathbf{X}_k \right) \right)_{jm}} \quad (10)$$

$$(\mathbf{Z}_k)_{jm} \leftarrow (\mathbf{Z}_k)_{jm} \frac{\beta \left(\sum_{p=1}^{k-1} ((\mathbf{G})_{kp} - (\mathbf{G})_{pk}) \mathbf{W}_{pk}^T \mathbf{X}_p + \rho \mathbf{X}_k \right)_{jm}}{\left(\beta \sum_{p=1}^{k-1} ((\mathbf{G})_{kp} - (\mathbf{G})_{pk}) \mathbf{D}_{pk2} \mathbf{Z}_k + \Theta_k + \rho \mathbf{Z}_k \right)_{jm}} \quad (11)$$

$$(\Theta_k)_{jm} \leftarrow (\Theta_k)_{jm} + \rho (\mathbf{Z}_k - \mathbf{X}_k)_{jm} \quad (12)$$

Algorithm 1 MuCSUn Based on Graph Regularization**Input:** \mathbf{Y} **Output:** \mathbf{A}, \mathbf{X}

- 1: **for** $i = 1$ to N **do**
- 2: calculate \mathbf{W} between all combinations between \mathbf{Y}_i and the others
- 3: find K nearest neighbors of \mathbf{Y}_i
- 4: prepare \mathbf{G}
- 5: initialize $\{\mathbf{A}_k, \mathbf{X}_k\}_{k \in \mathcal{V}_i}$ by ISU (\mathcal{V}_i is a set of the i th target and K neighbor images)
- 6: solve (6) by alternating updates of (7)–(12)
- 7: update $\{\mathbf{A}_i, \mathbf{X}_i\}$
- 8: **end for**
- 9: **return** $\{\mathbf{A}_i, \mathbf{X}_i\}_{i=1}^N$

signature matrix \mathbf{A}_k are augmented by constants defined by $\tilde{\mathbf{Y}}_k = [\mathbf{Y}_k^T \delta \mathbf{1}_P]^T$ and $\tilde{\mathbf{A}}_k = [\mathbf{A}_k^T \delta \mathbf{1}_P]^T$, where δ controls the impact of the constraint [35]. A moderate parameter value relaxes the constraint to some extent. The abundance sum-to-one constraints can also be explicitly included in the optimization, and the update rules can be derived by the augmented Lagrangian method. We adopt the former technique to avoid strict sum-to-one constraints, which do not properly reflect reality due to spectral variability.

The iterative process is terminated when the following two conditions are satisfied. The first one is the condition that the change ratio of the objective function O achieves a value below a given threshold ϵ_o , i.e., $\|\nabla O\|_2 \leq \epsilon_o O$, where ϵ_o is set to 10^{-3} in our experiments. The second one is the convergence of residuals for the equality constraints, i.e., $((\|\mathbf{A} - \mathbf{B}\|_F) / ((P \times M \times (K + 1))^{1/2})) \leq \epsilon_r$ and $((\|\mathbf{X} - \mathbf{Z}\|_F) / ((P \times M \times (K + 1))^{1/2})) \leq \epsilon_r$, where ϵ_r is set to 10^{-4} . The penalty parameters (σ and ρ) affect the convergence of the residuals and the choice of these parameters is an open question. In the literature, it has been recommended to use possibly different penalty parameters for improving the convergence while making performance less dependent on the initial choice. We adopt a parameter adjustment scheme in [63] that increases the penalty parameter with a factor τ only if the residual is not decreased by a factor $\mu < 1$, where τ and μ are set to 10 and 0.25, respectively, and the initial parameter is set to 10^{-5} . The Lagrange multipliers (Υ and Θ) are typically initialized as 0. For a practical utility, the maximum number of iterations is also used as the stopping criteria, which is set to 200 in the experiments.

The proposed algorithm for MuCSUn is summarized in Algorithm 1.

C. Atmospheric Normalization and Cross Calibration of SRFs

The estimation of the residual parameters and the relative SRFs represents the key to handling multisensor time-series data sets. In this section, we first introduce two atmospheric normalization methods to estimate the residual gains and offsets (\mathbf{c}_0 , \mathbf{c}_1). One method is based on spectral unmixing and the other is based on cross normalization. Next,

we present an image-based method for estimating relative SRFs.

1) *Atmospheric Normalization Based on Spectral Unmixing*: We assume that the relative SRFs (\mathbf{R}) and the initial endmember spectra (\mathbf{A}) are given. For example, \mathbf{R} is usually measured prelaunch and may be updated during in-flight calibration and monitoring. We suppose that an approximation of \mathbf{A} is determined using a spectral library or extracted from a master image (or images) by means of user interaction. If \mathbf{R} and \mathbf{A} are available, \mathbf{c}_1 and \mathbf{c}_0 can be obtained by the least-squares method after estimating \mathbf{X} . Expression (5) is thus rewritten as

$$\mathbf{Y} = \mathbf{RAX}^T + \text{diag}(\mathbf{c}_1)\mathbf{RAX}^T + \mathbf{c}_0\mathbf{1}_P^T + \mathbf{N}. \quad (13)$$

Assuming that $\mathbf{c}_0 \sim \mathcal{N}(\mathbf{0}, \sigma_0^2 \mathbf{I})$, $\mathbf{c}_1 \sim \mathcal{N}(\mathbf{0}, \sigma_1^2 \mathbf{I})$, and $\sigma_0, \sigma_1 \ll 1$, $\text{diag}(\mathbf{c}_1)\mathbf{RAX}^T$ and $\mathbf{c}_0\mathbf{1}_P^T$ can be approximated as Gaussian residuals. Therefore, we approximate \mathbf{X} by solving

$$\begin{aligned} \min_{\mathbf{X}} \quad & \|\mathbf{Y} - \mathbf{RAX}^T\|_F^2 \\ \text{s.t.} \quad & \mathbf{X} \geq \mathbf{0}. \end{aligned} \quad (14)$$

\mathbf{X} is obtained using the CLS method. The residual gain and offset for the i th band (c_{1i}, c_{0i}) are determined by

$$[1 + c_{1i} \quad c_{0i}]^T = (\tilde{\mathbf{X}}_i^T \tilde{\mathbf{X}}_i)^{-1} \tilde{\mathbf{X}}_i^T \mathbf{Y}^i \quad (15)$$

where $\tilde{\mathbf{X}}_i = [(\mathbf{RAX}^T)^i \quad \mathbf{1}_P]$. When the number of spectral bands (B) of the target image is large (e.g., \mathbf{Y} is an HS data set), the assumptions ($\mathbf{c}_0 \sim \mathcal{N}(\mathbf{0}, \sigma_0^2 \mathbf{I})$, $\mathbf{c}_1 \sim \mathcal{N}(\mathbf{0}, \sigma_1^2 \mathbf{I})$) are satisfied and therefore we can estimate the coefficients accurately.

2) *Image-Based Atmospheric Normalization*: The method described above causes large prediction errors when B is small (e.g., \mathbf{Y} is an MS data set) because $\text{diag}(\mathbf{c}_1)\mathbf{RAX}^T$ and $\mathbf{c}_0\mathbf{1}_P^T$ cannot be approximated as Gaussian residuals. In this case, we adopt image-based cross-normalization methods, which have been widely used in multitemporal studies [57], [58]. We prepare a reference image ($\mathbf{Z} \in \mathbb{R}^{B_0 \times P}$) that is already accurately corrected by the estimated residual parameters (e.g., HS data). We assume that there are unchanged pixels between the target and reference images. The relationship between the two images can be written as

$$\mathbf{Y}_{\mathcal{A}} = \text{diag}(\mathbf{1}_B + \mathbf{c}_1)\mathbf{RZ}_{\mathcal{A}} + \mathbf{c}_0\mathbf{1}_P^T + \mathbf{N}. \quad (16)$$

Here \mathcal{A} denotes a subset of unchanged pixels, which can be determined by similarity measures of spectral signatures between spatially corresponding pixels. If \mathbf{R} is available, \mathbf{c}_0 and \mathbf{c}_1 can be obtained by the least squares method. Considering that the reference image can still include errors due to nonoptimal atmospheric correction, the use of more than one reference image leads to better estimation of the coefficients. However, to satisfy the assumption of unchanged pixels, we need to select reference images close to the target image in the manifold of the time-series data set. Note that when \mathbf{A} is extracted from a single (master) image, its residual parameters can be regarded as ideal ($\mathbf{c}_0 = \mathbf{0}_B$ and $\mathbf{c}_1 = \mathbf{0}_B$); therefore, this image is suitable for being used as a reference for cross-normalization purposes.

3) *Cross Calibration of SRFs*: We consider now the image-based estimation of relative SRFs, particularly those of an MS imager spectrally resampled with the number of HS bands. Although prelaunch SRFs are usually available for spaceborne spectral imagers, image-based methods for estimating relative SRFs have been shown to be effective for data fusion purposes [59], mainly because a linear approximation of SRFs of the MS imager using those provided by the HS imager always includes errors, and furthermore, SRFs can change slightly on-board due to launch or secular change issues [60]. Now consider the problem of estimating the relative SRFs with residual gains ($\text{diag}(\mathbf{1}_B + \mathbf{c}_1)\mathbf{R}$) and offsets (\mathbf{c}_0) based on (16). The problem for each band can be expressed as

$$\begin{aligned} \min_{(1+c_{1i})\mathbf{R}^i, c_{0i}} \quad & \|\mathbf{Y}_{\mathcal{A}}^i - (1 + c_{1i})\mathbf{R}^i\mathbf{Z}_{\mathcal{A}} - c_{0i}\mathbf{1}_P^T\|_2^2 \\ \text{s.t.} \quad & (1 + c_{1i})\mathbf{R}^i \geq \mathbf{0}_{B_0}^T \end{aligned} \quad (17)$$

which can be solved via quadratic programming [61]. We assume that the residuals due to nonoptimal atmospheric correction have statistically no pattern, i.e., the mean of the residual gain for each band of the MS imager is equal to zero ($\bar{\mathbf{c}}_1 = \mathbf{0}_B$). Therefore, the relative SRFs can be obtained as $\mathbf{R} = (1/L) \sum_{k=1}^L (\text{diag}(\mathbf{1}_B + \mathbf{c}_1)\mathbf{R})_k$, where L is the number of images acquired by the MS imager.

The method for estimation of the residual parameters and relative SRFs presented in this section is summarized in Algorithm 2.

III. EXPERIMENT ON SYNTHETIC DATA

A. Synthetic Multisensor Time-Series Spectral Images

We use a set of synthetic multisensor time-series spectral images to numerically validate the proposed methodology. The synthetic data set was simulated using the abundance maps of the *Fractal 1* synthetic data [62]. The *Fractal 1* image is composed of nine endmembers; their abundance maps were generated from fractal patterns with the size of 100×100 pixels. To simulate realistic changes on the surface, we mainly consider seasonal changes and trend changes, which represent two major types of changes on the surface. We selected nine endmembers from the U.S. Geological Survey spectral library: *Grass*, *Dry grass*, *Oak*, *Soil*, *Melting snow*, *Water*, *Asphalt*, *Green house*, and *Concrete*. The reference abundance maps of endmembers #1–9 are used for (*Grass*, *Dry grass*), (*Dry grass*, (*Oak*, *Soil*)), (*Soil*, (*Grass*, *Melting snow*)), (*Water*, *Asphalt*), (*Green house*, *Soil*), and (*Concrete*, *Soil*), respectively, where (\cdot, \cdot) denotes a pair. Three pairs (*Grass*, *Dry grass*), (*Grass*, *Melting snow*), and (*Oak*, *Soil*) were used to simulate seasonal changes. We assume that *Grass* and *Oak* are foreground objects and *Dry grass*, *Melting snow*, and *Soil* are background objects. Seasonal abundance changes of foreground objects were simulated as the multiplication of periodic functions and the reference abundances. The expressions $(1 - \sin(2\pi t/365))/2$ and $(1 - \cos(2\pi t/365))/2$ were used as periodic functions for *Grass* and *Oak*, respectively, where t denotes the day on which the images were taken. We used the two different periodic functions to simulate different seasonal growth cycles

Algorithm 2 Atmospheric Normalization and Cross Calibration of SRFs

Input: \mathbf{Y}

Output: Corrected \mathbf{Y} , $\{\mathbf{R}_i\}_{i=1}^N$

```

1: for  $i = 1$  to  $N$  do
2:   if  $B_i = B_0$  then
3:      $\mathbf{R}_i = \text{diag}(\mathbf{1}_{B_0})$ 
4:     if initial  $\mathbf{A}_i$  is given from a master image then
5:       estimate  $\{\mathbf{c}_{0i}, \mathbf{c}_{1i}\}$  by the image-based method with
         the master image
6:     else
7:       estimate  $\{\mathbf{c}_{0i}, \mathbf{c}_{1i}\}$  by the spectral-unmixing-based
         method
8:     end if
9:     correct  $\mathbf{Y}_i$  by  $\text{diag}(\mathbf{1}_B + \mathbf{c}_{1i})^{-1}(\mathbf{Y}_i - \mathbf{c}_{0i}\mathbf{1}_P^T)$ 
10:    else
11:      estimate  $\{(\mathbf{1}_B + \mathbf{c}_1)\mathbf{R}\}_i, \mathbf{c}_{0i}\}$  by the image-based
        method
12:    end if
13:  end for
14: for  $i = 1$  to  $N$  do
15:   if  $B_i < B_0$  then
16:      $\mathbf{R}_i = \frac{1}{|S|} \sum_{k \in S} (\text{diag}(\mathbf{c}_1)\mathbf{R})_k$  where  $S$  is a subset data
       set taken by the same sensor as the  $i$ th image
17:     estimate  $\{\mathbf{c}_{0i}, \mathbf{c}_{1i}\}$  by the cross-normalization method
       with the reference images that have  $B_0$  bands
18:     correct  $\mathbf{Y}_i$  by  $\text{diag}(\mathbf{1}_B + \mathbf{c}_{1i})^{-1}(\mathbf{Y}_i - \mathbf{c}_{0i}\mathbf{1}_P^T)$ 
19:   end if
20: end for
21: return  $\{\mathbf{Y}_i, \mathbf{R}_i\}_{i=1}^N$ 

```

of vegetation. The residual abundances were added to the abundances of background objects. Other two pairs (*Green house*, *Soil*) and (*Concrete*, *Soil*) were selected for simulating trend changes defining green house and concrete as foreground objects and soil as background. The monotonic increasing function defined by $(t/(365 \times 5))$ was used to generate time-series abundance maps of green house and concrete. The residual abundances were added to the abundances of soil.

The SRFs of AVIRIS (bands 1–32, 36–96, 100–160, and 163–224) and Landsat-8 (bands 1–8) were used to simulate HS and MS images, respectively. Additive Gaussian noise with a signal-to-noise ratio of 100 was added to each temporal image. Nonoptimal atmospheric correction is simulated using a Gaussian random vector for the residual gains as $\mathbf{c}_1 \sim \mathcal{N}(\mathbf{0}, \sigma_1^2 \mathbf{I})$. σ_1 is set to 0.05 based on experimental results from real data, which will be shown in Section IV. \mathbf{c}_0 is set to $\mathbf{0}$ for simplicity. The revisit cycles of the HS and MS imagers were set to 16 and 27 days, respectively, which correspond to those of Landsat-8 and EnMAP. We consider two scenarios for data acquisition: 1) full acquisition, which assumes a clear sky for all images and 2) realistic acquisition, which assumes a clear sky for 30% of the observations. The total observation period is set to five years, and therefore, the total number of images is 68 and 115 for HS and MS images, respectively. Composite color images are shown

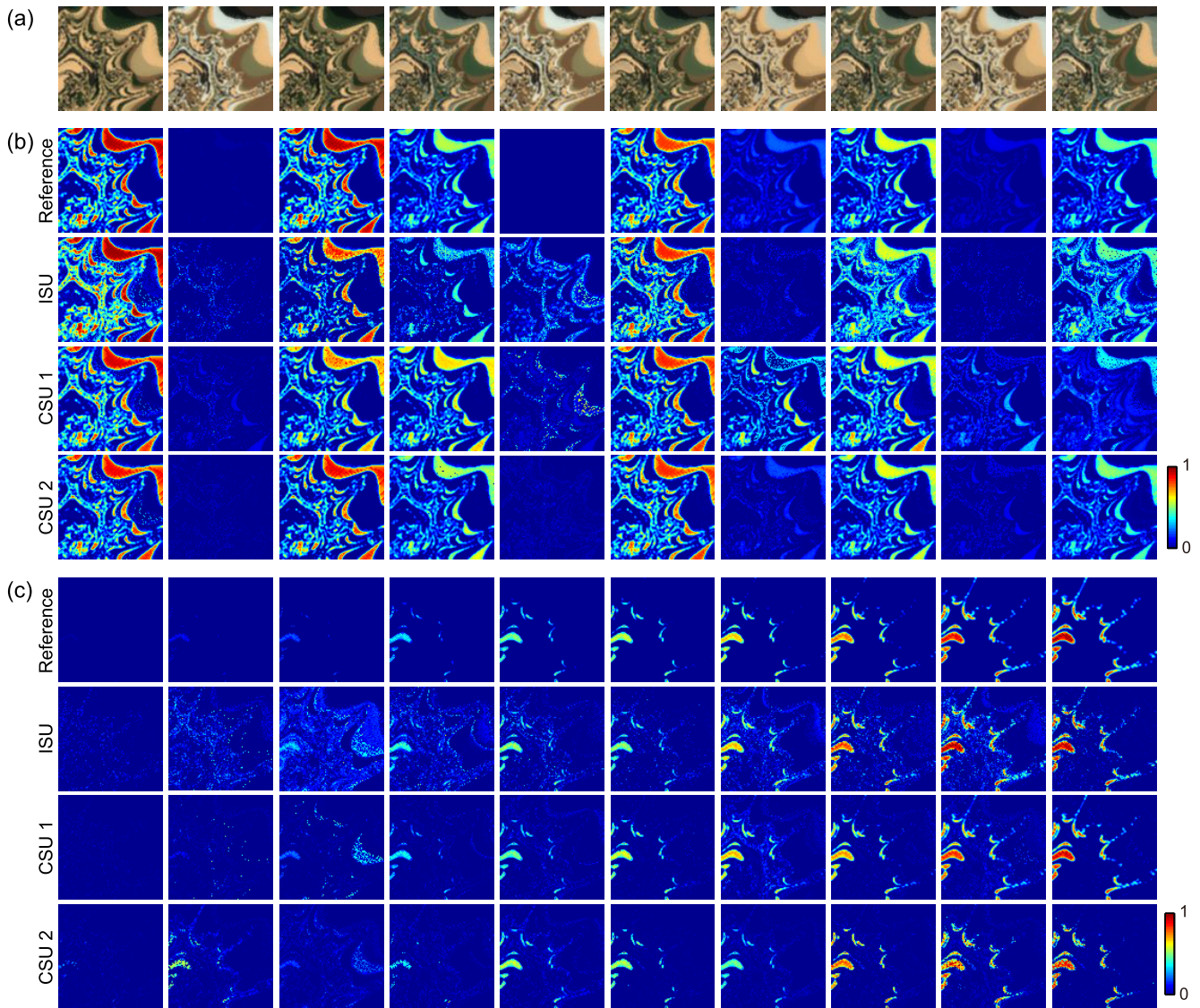


Fig. 2. (a) Color composites of ten images in the synthetic data set and their corresponding abundance maps of (b) *Grass* and (c) *Concrete*. Abundances of reference and estimated abundances obtained by ISU, CSU 1, and CSU 2 are shown from top to bottom in (b) and (c).

in Fig. 2(a) for ten examples. The corresponding reference abundances of *Grass* and *Concrete* are presented in the first row images of Fig. 2(b) and (c).

B. Experimental Results

In this experiment, we examine the efficacy of the following four points: 1) coupled spectral unmixing compared with ISU; 2) the use of multiple sensors compared with the use of a single sensor; 3) manifold-based coupling compared with sequential coupling; and 4) atmospheric normalization. To investigate the first and third points, we use three methods: 1) ISU based on the CLS method; 2) coupled spectral unmixing with sequential coupling (CSU 1); and 3) coupled spectral unmixing with manifold-based coupling (CSU 2). ISU can be seen as a special case of MuCSUn that performs only the initialization process in line 5 in Algorithm 1. CSU 1 and CSU 2 are two variations of MuCSUn and their difference

is defined only by the preparation process of the adjacency matrix \mathbf{G} in line 4 in Algorithm 1. To investigate the second point, we perform these methods on three different data sets: 1) only HS images; 2) only MS images; and 3) HS and MS images. For the last point, we conduct all experiments with and without atmospheric normalization. To fairly validate our technical contributions, we simplify our algorithm by setting $\alpha = 0$ and $\gamma = 0$, and \mathbf{A} is given and fixed. The number of neighbors is two and $\beta = 1$.

Table I shows the average root-mean-square errors (RMSEs) of abundances, defined by $(1/N) \sum_{i=1}^N \|\mathbf{X}_i - \tilde{\mathbf{X}}_i\|_F / \sqrt{PM}$, with atmospheric normalization. The results were obtained for three data sets using three considered methods in the two scenarios. For the realistic data acquisition scenario, we show the average results of ten Monte Carlo trials obtained after selecting 30% of the observations. Note that only the unmixing accuracy of MS images is shown for the third data set, because

TABLE I

AVERAGE RMSEs OF ABUNDANCES OBTAINED AFTER ATMOSPHERIC NORMALIZATION FROM THREE DATA SETS OF SYNTHETIC TIME-SERIES SPECTRAL IMAGES, i.e., ONLY HS DATA (68 IMAGES), ONLY MS DATA (115 IMAGES), AND BOTH HS AND MS DATA (183 IMAGES) USING ISU, COUPLED SPECTRAL UNMIXING WITH SEQUENTIAL COUPLING (CSU 1), AND MANIFOLD-BASED COUPLING (CSU 2). RMSEs FOR ONLY MS DATA ARE SHOWN FOR THE LAST DATA SET

Dataset	HS		MS		MS (coupled with HS)	
	Ideal	Realistic	Ideal	Realistic	Ideal	Realistic
ISU	0.013588	0.013336	0.06987	0.069512	0.06987	0.069512
CSU 1	0.012392	0.013559	0.082818	0.068334	0.019508	0.040315
CSU 2	0.012309	0.012407	0.064022	0.064740	0.022227	0.031097

TABLE II

AVERAGE RMSEs OF ABUNDANCES OBTAINED BEFORE ATMOSPHERIC NORMALIZATION FROM THREE DATA SETS OF SYNTHETIC TIME-SERIES SPECTRAL IMAGES, i.e., ONLY HS DATA (68 IMAGES), ONLY MS DATA (115 IMAGES), AND BOTH HS AND MS DATA (183 IMAGES) USING ISU, COUPLED SPECTRAL UNMIXING WITH SEQUENTIAL COUPLING (CSU 1), AND MANIFOLD-BASED COUPLING (CSU 2). RMSEs FOR ONLY MS DATA ARE SHOWN FOR THE LAST DATA SET

Dataset	HS		MS		MS (coupled with HS)	
	Ideal	Realistic	Ideal	Realistic	Ideal	Realistic
ISU	0.028181	0.028526	0.11484	0.11719	0.11484	0.11719
CSU 1	0.025268	0.026195	0.1161	0.12110	0.086309	0.092507
CSU 2	0.025552	0.025896	0.11538	0.11840	0.049207	0.052016

only MS images can gain benefits, whereas the results of HS images are the same as the first data set. The coupled spectral unmixing algorithms show better performance compared with ISU. The unmixing accuracy of MS data is highly improved by solving unmixing problems with HS data in a coupled basis. This demonstrates the benefit of using multiple sensors for spectral unmixing, or more precisely, spectral unmixing of MS data can be greatly improved owing to the support of neighboring HS data. Coupled spectral unmixing based on manifold-based coupling outperforms estimations based on sequential coupling in many cases, particularly in the realistic data acquisition scenarios. This suggests that manifold-based coupling leads to more accurate and robust unmixing results than sequential coupling. Coupled spectral unmixing with sequential coupling performs well in ideal scenarios because sequential neighbors with high temporal resolution represent neighbors in the manifold of time-series data well. On the other hand, if temporal resolution of time-series data is limited to realistic scenarios, manifold-based coupling is required because sequential neighbors do not always represent neighbors in the manifold.

Table II shows the unmixing accuracy obtained without atmospheric normalization. The unmixing accuracies greatly decrease in all scenarios with all data sets and methods. This proves the importance of the estimation and correction of the residual parameters. Major trends among the three methods are similar to those observed in Table I, whereas it can be seen that there is no improvement obtained by coupled spectral unmixing for the MS-only data set. MS

unmixing problems are severely ill posed before atmospheric normalization, and therefore, ISU results in large estimation errors. Since the proposed methods use the result of ISU for initialization, they converge to inaccurate local optima possibly worse than the initial solution. The differences in accuracy between Tables I and II are larger than those between individual and coupled approaches presented. This implies that atmospheric normalization with the estimation of the residual parameters has a larger impact than the coupled spectral unmixing algorithm.

Fig. 2(b) and (c) presents reference abundance maps of *Grass* and *Concrete* for a subset of time-series data with one trial of the realistic acquisition scenario and the corresponding estimated abundance maps obtained by the three methods. *Grass* and *Concrete* are defined as endmembers with seasonal and trend changes, respectively, as shown in the changes of abundances. Serial day numbers of the subset are 113, 289, 433, 737, 1009, 1137, 1313, 1473, 1697, and 1825, which are all simulated as observed by the MS imager. In Fig. 2(b), the coupled spectral unmixing methods show better resemblance to the reference compared with ISU. In particular, manifold-based coupling (CSU 2) exhibits the best results. In contrast, in Fig. 2(c), sequential coupling (CSU 1) shows the best resemblance, whereas both CSU 1 and CSU 2 outperform ISU. These results imply that manifold-based coupling can better capture seasonal changes and sequential coupling is more suitable for detection of trend changes.

Fig. 3 shows time-series plots of abundances at four example points. The coupled spectral unmixing methods show robust and stable estimation results. Manifold-based coupling results in better estimation of seasonal abundance changes, as shown in the abundances of *Oak* and *Soil* of the first point [see Fig. 3(a)]. Sequential coupling leads to good detection of trend changes, as shown in the abundances of *Soil* of the third point [see Fig. 3(c)] and *Soil* and *Green house* of the fourth point [see Fig. 3(d)]. These results also confirm the advantages of manifold-based and sequential coupling in the proposed methodology.

Finally, we investigate the effect of the parameter β on the performance in the experiment for the data set composed of both HS and MS images with atmospheric normalization. Fig. 4(a) and (b) plots the average RMSE of abundances as a function of β for CSU 1 and CSU 2 under the ideal and realistic data acquisition scenarios, respectively. The choice of β affects the results and the sensitivity trend depends on temporal resolution of the time-series data set. In the ideal scenario, both CSU 1 and CSU 2 perform well and stable when $\beta \geq 1$. A similar sensitivity trend is observed in the realistic scenario when $\beta \leq 10^{-1}$; however, the performance decreases as β increases larger than 1. This result indicates that a moderate use of graph regularization (e.g., $\beta = 1$) is appropriate in the realistic scenario because the neighboring images include surface changes to some extent compared with a target image.

In the experiments conducted using synthetic data, our findings are summarized as follows.

- 1) Atmospheric normalization with the estimation of residual parameters highly improves the unmixing accuracy;

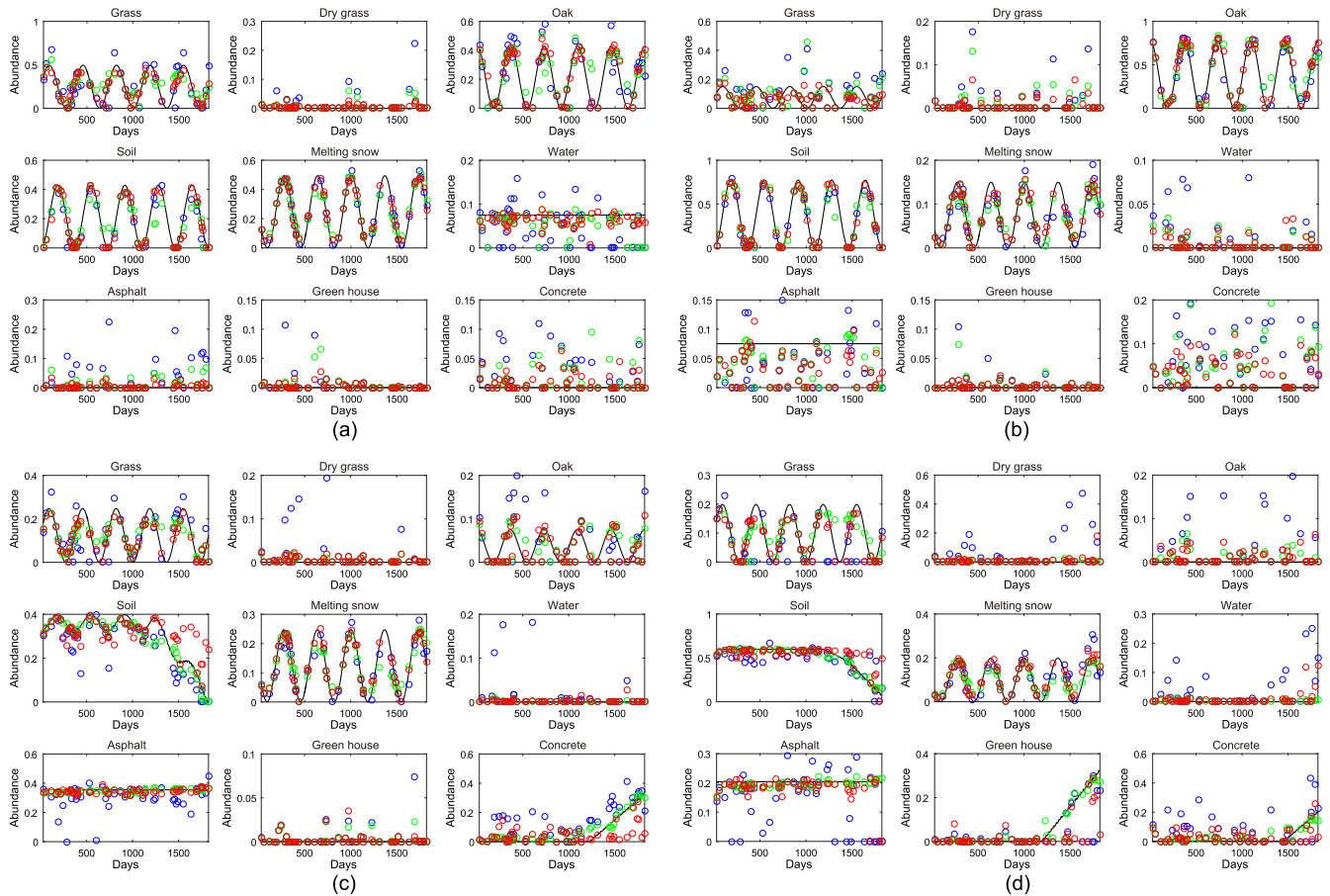


Fig. 3. Time-series plots of abundances for nine endmembers at four example points obtained by (a)–(d) ISU (blue circles), CSU 1 (green circles), CSU 2 (red circles), and reference (black curves), respectively.

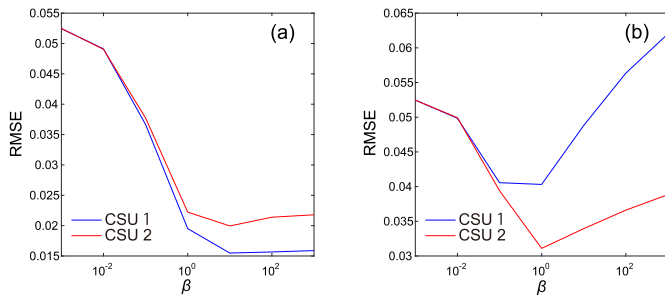


Fig. 4. Sensitivity to the change of the parameter β under (a) ideal and (b) realistic data acquisition scenarios.

therefore, it is required as preprocessing in time-series spectral analysis.

- 2) Coupled spectral unmixing outperforms ISU.
- 3) The use of multiple sensors can improve spectral unmixing of MS data.
- 4) Manifold-based coupling is suitable for capturing seasonal changes, whereas sequential coupling is better able to detect trend changes.

IV. EXPERIMENT ON REAL DATA

A. Time-Series Hyperion and Landsat-8 Images

To validate the proposed methodology using real data, an experiment was performed on a multisensor time-series data set composed of Hyperion and Landsat-8 data. The data

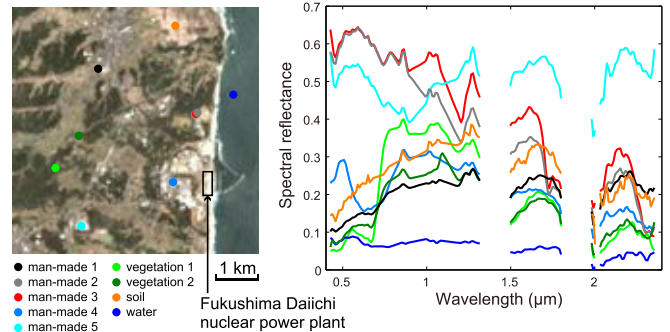


Fig. 5. Location and spectral signatures of endmembers obtained from Hyperion data taken on April 29, 2012 near the Fukushima Daiichi nuclear power plant.

set includes 11 Hyperion images and 22 Landsat-8 images acquired from August 13, 2011 to October 9, 2015 over Fukushima, Japan, after the Great East Japan earthquake on March 11, 2011. The study scene covers the Fukushima Daiichi Nuclear Power Station ($37^{\circ}25'16''$, $141^{\circ}1'58''$) and its surrounding area [see Fig. 5 (left)], where visiting on site is forbidden. Since the earthquake, storage tanks have been built to store polluted water and many of the abandoned areas have been covered by weeds.

All the images were first coregistered using geocoordinate information and further registered using phase-correlation-based image matching in case a misregistration of more than

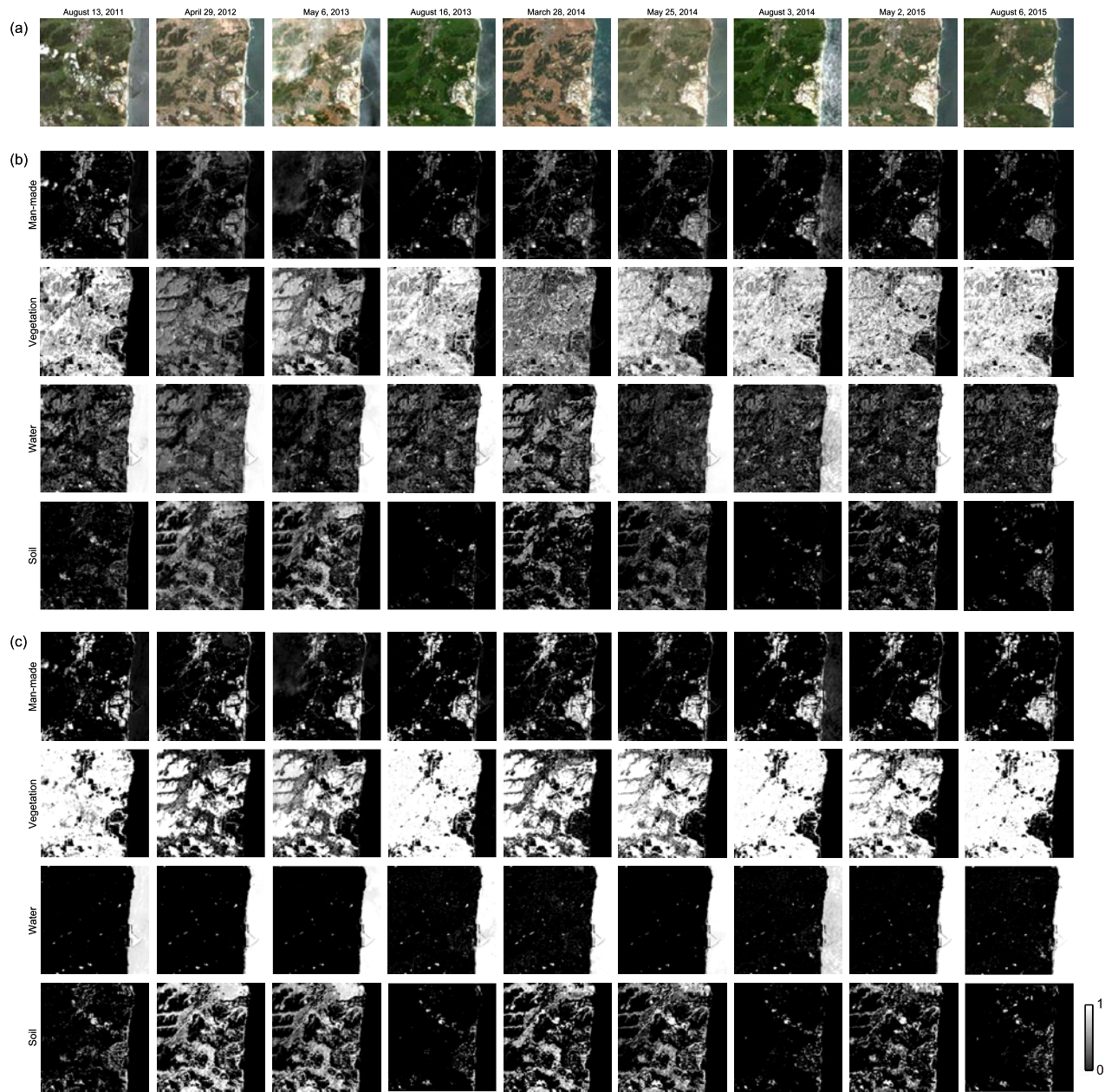


Fig. 6. (a) Color composite images. Abundance maps of man-made, vegetation, water, and soil obtained by (b) ISU and (c) coupled spectral unmixing.

TABLE III
DATA ACQUISITION DATES AND SENSORS

2011		2013		2014		2015	
Date	Sensor	Date	Sensor	Date	Sensor	Date	Sensor
August 13	Hyperion	January 29	Hyperion	January 7	Landsat-8	February 27	Landsat-8
December 18	Hyperion	February 24	Hyperion	January 23	Landsat-8	March 15	Landsat-8
		May 6	Hyperion	February 24	Landsat-8	March 31	Landsat-8
		August 16	Landsat-8	March 28	Landsat-8	May 2	Hyperion
		September 1	Landsat-8	April 13	Landsat-8	May 18	Landsat-8
		October 17	Landsat-8	May 25	Hyperion	July 9	Hyperion
		October 27	Hyperion	May 31	Landsat-8	July 21	Landsat-8
		November 20	Landsat-8	June 16	Landsat-8	August 6	Landsat-8
				July 2	Landsat-8	October 9	Landsat-8
				July 12	Hyperion		
				August 3	Landsat-8		
				December 25	Landsat-8		

one pixel is detected [64]. Image registration was performed only by shifting a whole image at a pixel scale to avoid interpolation while keeping the same spatial resolution. We used

ATCOR for atmospheric correction [65]. For the Hyperion data, we used 156 bands (bands 8–57, 79–117, 135–165, 183–185, and 188–220) after removing bands that include only zero values and strong water vapor absorption. For the Landsat-8 data, we used bands 1–7 for the experiment. The data acquisition dates and sensors are summarized in Table III. Color composite images of a subset of the data set after atmospheric normalization are shown in Fig. 6(a).

B. Experimental Results

In this paper, we considered the Hyperion image taken on April 29, 2012 as the master image. VCA was used to extract endmembers from this image. Spectral smoothing was performed to reduce spikes due to nonoptimal atmospheric correction. The spectral signatures were manually labeled,

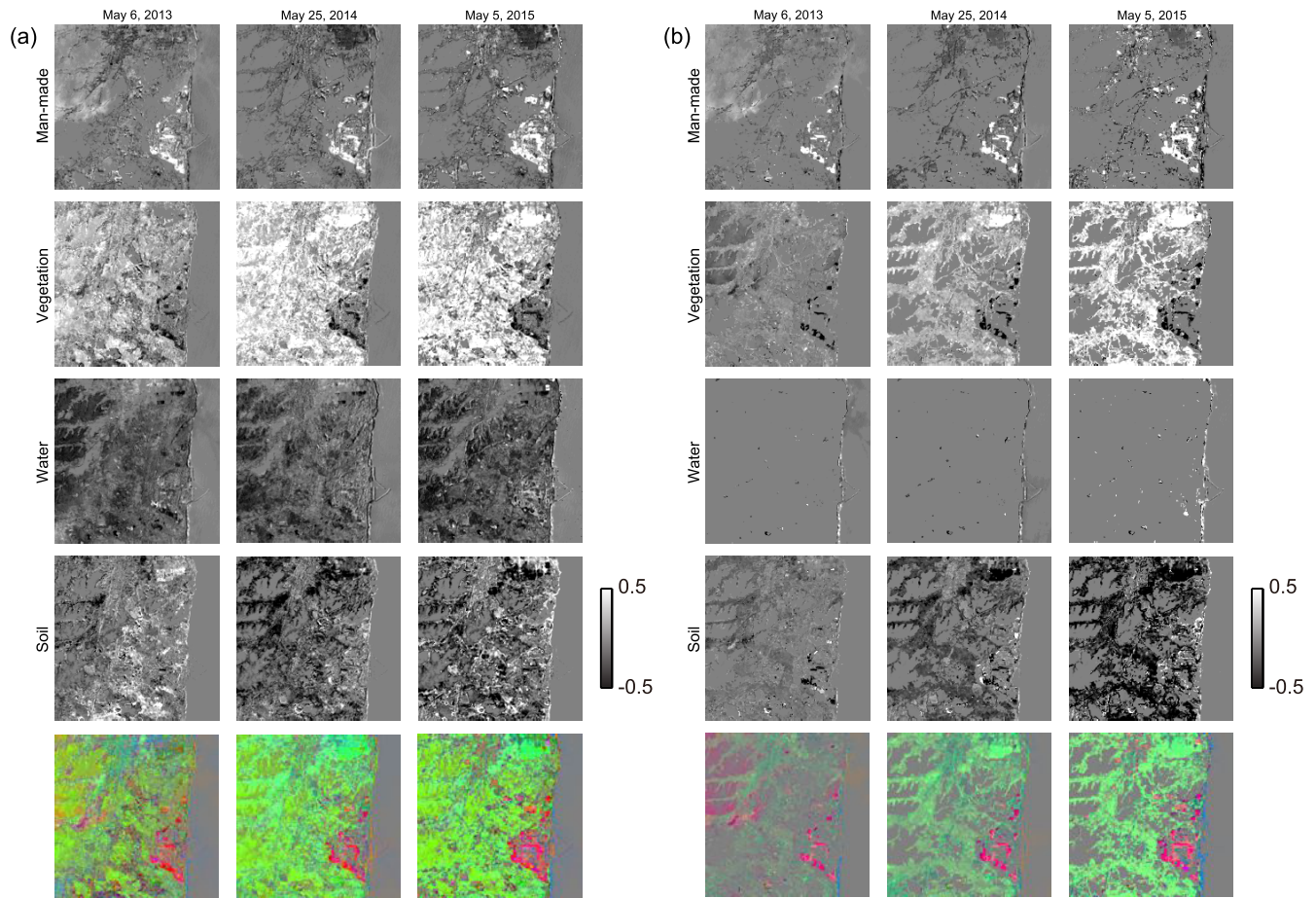


Fig. 7. Abundance changes on May 6, 2013, May 25, 2014, and May 2, 2015 compared with April 29, 2012 obtained by (a) ISU and (b) coupled spectral unmixing. The grayscale images correspond to abundance maps of man-made objects, vegetation, water, and soil in the first row to the fourth row and the color composite images in the fifth row are made up of abundance difference maps of man-made, vegetation, and soil for red patches, green patches, and blue patches, respectively.

resulting in nine endmembers: water, soil, two kinds of vegetation, and five different man-made objects. Fig. 5 presents the spectral signatures of these nine endmembers and their locations in the scene. \mathbf{A} was fixed and γ was set to 0 for two reasons. First, temporal spectral variability in the studied time-series data set was greatly affected by atmospheric conditions such as clouds. By fixing \mathbf{A} , we prevented convergence of endmembers to spectral signatures significantly affected by clouds. Second, temporal spectral variability of surface objects was well represented by using the extracted endmembers when our analysis is focused on discriminating coarse categories (e.g., water, soil, vegetation, and man-made objects). α was set to 0.05 as the average value of estimated α s for all the images using the criterion given in (4). We set $\beta = 1$ based on the parameter sensitivity analysis in Section III-B. The number of neighbors was set to two.

Fig. 6(b) and (c) shows the nine temporal abundance maps obtained by ISU and the proposed methodology with manifold-based coupling, respectively. Here, the nine endmembers are classified into four categories, i.e., water, soil, vegetation, and man-made. The proposed method shows more stable results compared with ISU. For example, in Fig. 6(b),

the abundances of man-made objects are highly influenced by thin clouds (May 6, 2013) and waves (August 3, 2014). These effects are majorly mitigated by the proposed method, as shown in the corresponding abundance maps of Fig. 6(c), where seasonal changes of vegetation and soil in abundances are clearly exhibited. Although ISU failed to estimate the abundances of the Landsat-8 data set taken on March 26, 2014, the coupled spectral unmixing method provided stable results. In Fig. 6(b), large abundance errors corresponding to water false positive estimations appear in the land area as a result of the strict sum-to-one constraint.

Fig. 7 gives an example of class-specific change detection using the unmixing results obtained from the four temporal Hyperion images. Fig. 7(a) and (b) depicts the results obtained by ISU and coupled spectral unmixing, respectively. The abundance changes on May 6, 2013, May 25, 2014, and May 2, 2015 (compared with April 29, 2012) are presented in the grayscale images from the first row to the fourth row for man-made objects, vegetation, water, and soil, respectively. The images in the last row of Fig. 7(a) and (b) are color composite images using abundance difference maps of man-made objects, vegetation, and soil for red patches, green

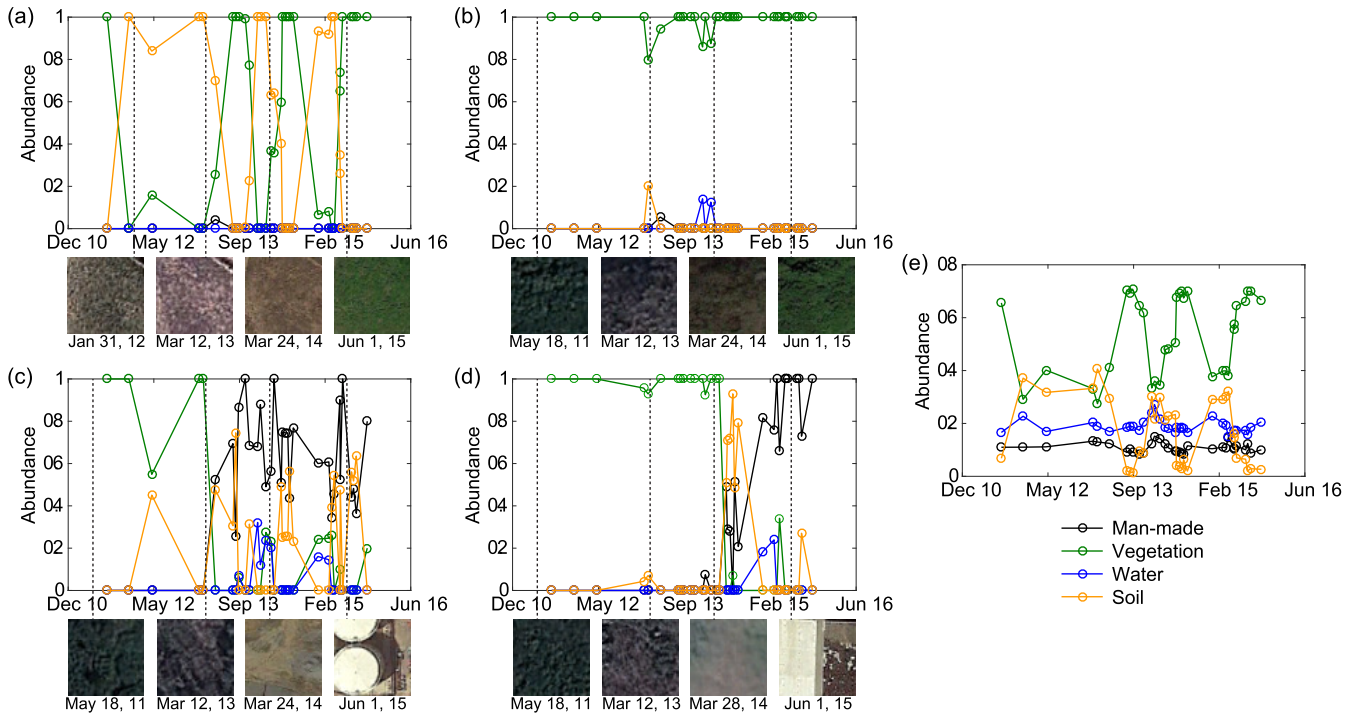


Fig. 8. Time-series plots of abundances for four categories obtained from 33 Hyperion and Landsat-8 images using (a)–(d) four example points and (e) those of average values in the study area. Four temporal high-resolution images at each point obtained from Google Earth are shown in (a)–(d).

patches, and blue patches, respectively, to visualize class-specific changes. For example, the *magenta*, *green*, *orange*, and *purple* patches indicate the changes from vegetation to man-made, from soil to vegetation, from soil to man-made, and from vegetation to soil, respectively.

In Fig. 7(a), it can be seen that there are too many overall abundance changes obtained by ISU. In contrast, Fig. 7(b) shows that the proposed method shows stable and reasonable results for the abundance changes. For example, in Fig. 7(a), it can be seen that the estimated abundances of vegetation change in evergreen forests, which are always shown by green patches in Fig. 6(a) (despite the fact that the actual abundance values do not significantly change). The proposed method shows stable results in evergreen forests, resulting in no change, and a gradual increase of vegetation can be visualized in areas (e.g., abandoned farmland) covered by deciduous plants (e.g., weeds), as illustrated in Fig. 7(b). On the other hand, the coupled spectral unmixing algorithm shows a gradual decrease of soil in these areas, whereas the abundance changes of soil obtained by ISU are hard to interpret. These results indicate that ISU results in unstable estimation of abundances due to spectral variability, including the effects of nonoptimal atmospheric correction. They further indicate that the coupled spectral unmixing method is able to mitigate this instability by adding regularization on abundances, so that similar pixels in neighborhood images in the manifold of time-series data have similar abundances. In the color composites representing abundance changes obtained by the proposed method, trees that have been cut down to increase the number of water storage tanks in and around the power plant are clearly visualized as *magenta* and *purple* pixels. The increase of

vegetation may be attributed to the growth of weeds owing to seasonal differences, as well as the yearly expansion of weeds in the abandoned farmland.

Fig. 8 presents time-series plots of abundances of four categories obtained from all the 33 Hyperion and Landsat-8 images using four example pixels [see Fig. 8(a)–(d)] and those of average values in the study area [see Fig. 8(e)]. Four temporal high-resolution images at each point (30×30 m) obtained from Google Earth are also shown in Fig. 8(a)–(d). In Fig. 8(a), seasonal changes of abundances between vegetation and soil show the existence of deciduous plants. Fig. 8(b) shows the high abundance of vegetation throughout the year, which demonstrates that the pixel is covered by evergreens. In Fig. 8(c) and (d), we can clearly observe the effects of deforestation and construction of man-made objects. In particular, Fig. 8(d) depicts the change of the surface from vegetation to soil to man-made objects. All the high-resolution images are consistent with the time-series plots of abundances, indicating the validity of the results of MuCSUn. In Fig. 8(e), we can find seasonal changes in abundance between vegetation and soil and relatively stable abundances of water and man-made objects. Minimal abundances of vegetation gradually increase during the four years, which implies the increase of weeds in the abandoned areas. This analysis of time-series plots of abundances has the potential to improve understanding of dynamic changes on the surface.

V. CONCLUSION

We proposed a framework for spectral unmixing of multisensor time-series spectral data. The proposed framework, called MuCSUn, provides robust and stable unmixing

solutions beyond data modalities due to the different spectral characteristics of imagers and the effects of nonoptimal atmospheric correction. A single unmixing problem is jointly solved with other unmixing problems in its neighborhood in the manifold of the time-series data set. Multiple unmixing problems are coupled via regularization on graphs between the local images. We also introduced methods for atmospheric normalization and cross calibration of SRFs. Quantitative validation was performed with synthetic time-series data composed of HS and MS images, including trend and seasonal changes and residual gains. The experiment demonstrated the efficacy of the proposed methodology. Atmospheric normalization showed large improvements in the accuracy of spectral unmixing, which suggests its importance as preprocessing in spectral unmixing of multisensor time-series spectral data. The coupled spectral unmixing algorithm also improved the unmixing accuracy compared with ISU. Spectral unmixing problems involving MS images particularly benefitted from the use of multisensor data in the context of our proposed methodology. Our methodology was applied to a real data set composed of 11 Hyperion and 22 Landsat-8 images and showed robust and stable results visualizing class-specific changes at a subpixel scale. These findings suggest that the proposed framework can contribute to the synergetic use of spaceborne HS and MS imagers for understanding dynamic changes on the surface.

In our future research, we intend to concentrate on end-member extraction from multisensor time-series spectral data learning temporal spectral variability. More experiments on real data and additional applications will be explored to verify the efficacy of MuCSUn.

APPENDIX

The objective function in (6) can be rewritten as

$$\begin{aligned}
O(\mathbf{A}, \mathbf{X}, \mathbf{B}, \mathbf{Z}) &= \frac{1}{2} \sum_{k=1}^{K+1} \text{Tr}((\mathbf{Y}_k - \mathbf{A}_k \mathbf{X}_k^T)(\mathbf{Y}_k - \mathbf{A}_k \mathbf{X}_k^T)^T) \\
&+ \alpha \sum_{k=1}^{K+1} \mathbf{1}_p^T \mathbf{X}_k^{1/2} \mathbf{1}_M + \frac{1}{2} \beta \sum_{p=1}^K \sum_{q=p+1}^{K+1} \\
&((\mathbf{G})_{pq}(\mathbf{G})_{qp}(\text{Tr}(\mathbf{X}_p^T \mathbf{D}_{pq1} \mathbf{X}_p) + \text{Tr}(\mathbf{X}_q^T \mathbf{D}_{pq2} \mathbf{X}_q) \\
&- 2\text{Tr}(\mathbf{X}_p^T \mathbf{W}_{pq} \mathbf{X}_q)) + ((\mathbf{G})_{qp} - (\mathbf{G})_{pq}) \\
&\times (\text{Tr}(\mathbf{X}_p^T \mathbf{D}_{pq1} \mathbf{X}_p) + \text{Tr}(\mathbf{Z}_q^T \mathbf{D}_{pq2} \mathbf{Z}_q) \\
&- 2\text{Tr}(\mathbf{X}_p^T \mathbf{W}_{pq} \mathbf{Z}_q))) + \gamma \sum_{p=1}^K \sum_{q=p+1}^{K+1} \\
&((\mathbf{G})_{pq}(\mathbf{G})_{qp} \text{Tr}(\mathbf{R}_{pq} \mathbf{A}_q - \mathbf{A}_p)(\mathbf{R}_{pq} \mathbf{A}_q - \mathbf{A}_p)^T) \\
&+ ((\mathbf{G})_{qp} - (\mathbf{G})_{pq}) \text{Tr}((\mathbf{R}_{pq} \mathbf{B}_q - \mathbf{A}_p)(\mathbf{R}_{pq} \mathbf{B}_q - \mathbf{A}_p)^T)). \tag{18}
\end{aligned}$$

Let $(\Phi_k)_{jm}$, $(\Psi_k)_{im}$, $(\Theta_k)_{jm}$, and $(\Upsilon_k)_{im}$ be the Lagrange multiplier for constraint $(\mathbf{X}_k)_{jm} \geq 0$ (nonnegativity of abundances), $(\mathbf{A}_k)_{im} \geq 0$ (nonnegativity of endmembers), $(\mathbf{X}_k)_{jm} = (\mathbf{Z}_k)_{jm}$ (consistency of auxiliary variables \mathbf{Z} with

\mathbf{X}), and $(\mathbf{A}_k)_{im} = (\mathbf{B}_k)_{im}$ (consistency of auxiliary variables \mathbf{B} with \mathbf{A}), respectively, then the augmented Lagrangian without the abundance sum-to-one constraint is given by

$$\begin{aligned}
L_c(\mathbf{A}, \mathbf{X}, \mathbf{B}, \mathbf{Z}, \Phi, \Psi, \Theta, \Upsilon) &= \frac{1}{2} \sum_{k=1}^{K+1} \text{Tr}((\mathbf{Y}_k - \mathbf{A}_k \mathbf{X}_k^T)(\mathbf{Y}_k - \mathbf{A}_k \mathbf{X}_k^T)^T) \\
&+ \alpha \sum_{k=1}^{K+1} \mathbf{1}_p^T \mathbf{X}_k^{1/2} \mathbf{1}_M + \frac{1}{2} \beta \sum_{p=1}^K \sum_{q=p+1}^{K+1} \\
&((\mathbf{G})_{pq}(\mathbf{G})_{qp}(\text{Tr}(\mathbf{X}_p^T \mathbf{D}_{pq1} \mathbf{X}_p) + \text{Tr}(\mathbf{X}_q^T \mathbf{D}_{pq2} \mathbf{X}_q) \\
&- 2\text{Tr}(\mathbf{X}_p^T \mathbf{W}_{pq} \mathbf{X}_q)) + ((\mathbf{G})_{qp} - (\mathbf{G})_{pq}) \\
&\times (\text{Tr}(\mathbf{X}_p^T \mathbf{D}_{pq1} \mathbf{X}_p) + \text{Tr}(\mathbf{Z}_q^T \mathbf{D}_{pq2} \mathbf{Z}_q) \\
&- 2\text{Tr}(\mathbf{X}_p^T \mathbf{W}_{pq} \mathbf{Z}_q))) + \gamma \sum_{p=1}^K \sum_{q=p+1}^{K+1} \\
&((\mathbf{G})_{pq}(\mathbf{G})_{qp} \text{Tr}((\mathbf{R}_{pq} \mathbf{A}_q - \mathbf{A}_p)(\mathbf{R}_{pq} \mathbf{A}_q - \mathbf{A}_p)^T) \\
&+ ((\mathbf{G})_{qp} - (\mathbf{G})_{pq}) \text{Tr}((\mathbf{R}_{pq} \mathbf{B}_q - \mathbf{A}_p)(\mathbf{R}_{pq} \mathbf{B}_q - \mathbf{A}_p)^T)) \\
&- \sum_{k=1}^{K+1} \text{Tr}(\Phi_k \mathbf{X}_k^T) - \sum_{k=1}^{K+1} \text{Tr}(\Psi_k \mathbf{A}_k^T) \\
&+ \sum_{k=1}^{K+1} \text{Tr}(\Theta_k (\mathbf{Z}_k - \mathbf{X}_k)^T) \\
&+ \sum_{k=1}^{K+1} \frac{\rho}{2} \text{Tr}((\mathbf{Z}_k - \mathbf{X}_k)(\mathbf{Z}_k - \mathbf{X}_k)^T) \\
&+ \sum_{k=1}^{K+1} \text{Tr}(\Upsilon_k (\mathbf{B}_k - \mathbf{A}_k)^T) \\
&+ \sum_{k=1}^{K+1} \frac{\sigma}{2} \text{Tr}((\mathbf{B}_k - \mathbf{A}_k)(\mathbf{B}_k - \mathbf{A}_k)^T). \tag{19}
\end{aligned}$$

The partial derivatives of L_c with respect to \mathbf{A}_k , \mathbf{B}_k , $\mathbf{X}_k > \mathbf{0}$, and \mathbf{Z}_k are

$$\begin{aligned}
\frac{\partial L_c}{\partial \mathbf{A}_k} &= -\mathbf{Y}_k \mathbf{X}_k + \mathbf{A}_k \mathbf{X}_k^T \mathbf{X}_k - \Psi_k - \Upsilon_k + \sigma (\mathbf{A}_k - \mathbf{B}_k) \\
&+ \gamma \left(\sum_{p=1}^{k-1} (\mathbf{G})_{pk} (\mathbf{G})_{kp} (\mathbf{R}_{pk}^T \mathbf{R}_{pk} \mathbf{A}_k - \mathbf{R}_{pk}^T \mathbf{A}_p) \right. \\
&+ \sum_{q=k+1}^{K+1} ((\mathbf{G})_{kq} (\mathbf{G})_{qk} (-\mathbf{R}_{kq} \mathbf{A}_q + \mathbf{A}_k) \\
&+ ((\mathbf{G})_{qk} - (\mathbf{G})_{kq}) (-\mathbf{R}_{kq} \mathbf{B}_q + \mathbf{A}_k)) \left. \right) \tag{20}
\end{aligned}$$

$$\begin{aligned}
\frac{\partial L_c}{\partial \mathbf{B}_k} &= \gamma \sum_{p=1}^{k-1} ((\mathbf{G})_{kp} - (\mathbf{G})_{pk}) (\mathbf{R}_{pk}^T \mathbf{R}_{pk} \mathbf{B}_k - \mathbf{R}_{pk}^T \mathbf{A}_p) \\
&+ \Upsilon_k + \sigma (\mathbf{B}_k - \mathbf{A}_k) \tag{21}
\end{aligned}$$

$$\begin{aligned}
 \frac{\partial L_c}{\partial \mathbf{X}_k} &= -\mathbf{Y}_k^T \mathbf{A}_k + \mathbf{X}_k \mathbf{A}_k^T \mathbf{A}_k + \alpha \mathbf{X}_k^{-1/2} - \Phi_k - \Theta_k \\
 &+ \rho (\mathbf{X}_k - \mathbf{Z}_k) \\
 &+ \beta \left(\sum_{p=1}^{k-1} (\mathbf{G})_{pk} (\mathbf{G})_{kp} (\mathbf{D}_{pk2} \mathbf{X}_k - \mathbf{W}_{pk}^T \mathbf{X}_p) \right. \\
 &\quad + \sum_{q=k+1}^{K+1} ((\mathbf{G})_{kq} (\mathbf{G})_{qk} (\mathbf{D}_{kq1} \mathbf{X}_k - \mathbf{W}_{kq} \mathbf{X}_q) \\
 &\quad \left. + ((\mathbf{G})_{qk} - (\mathbf{G})_{kq}) (\mathbf{D}_{kq1} \mathbf{X}_k - \mathbf{W}_{kq} \mathbf{Z}_q) \right) \quad (22)
 \end{aligned}$$

$$\begin{aligned}
 \frac{\partial L_c}{\partial \mathbf{Z}_k} &= \beta \sum_{p=1}^{k-1} ((\mathbf{G})_{kp} - (\mathbf{G})_{pk}) (\mathbf{D}_{pk2} \mathbf{Z}_k - \mathbf{W}_{pk}^T \mathbf{X}_p) + \Theta_k \\
 &+ \rho (\mathbf{Z}_k - \mathbf{X}_k). \quad (23)
 \end{aligned}$$

L_c is continuously differentiable under $\mathbf{X} > \mathbf{0}$, and the *Karush–Kuhn–Tucker* (KKT) conditions are satisfied. Using the KKT conditions, the following equations are obtained:

$$\begin{aligned}
 &-(\mathbf{Y}_k \mathbf{X}_k)_{im} (\mathbf{A}_k)_{im} + (\mathbf{A}_k \mathbf{X}_k^T \mathbf{X}_k)_{im} (\mathbf{A}_k)_{im} - (\Upsilon_k)_{im} (\mathbf{A}_k)_{im} \\
 &+ \gamma \left(\sum_{p=1}^{k-1} (\mathbf{G})_{pk} (\mathbf{G})_{kp} (\mathbf{R}_{pk}^T \mathbf{R}_{pk} \mathbf{A}_k - \mathbf{R}_{pk}^T \mathbf{A}_p)_{im} (\mathbf{A}_k)_{im} \right. \\
 &\quad + \sum_{q=k+1}^{K+1} ((\mathbf{G})_{kq} (\mathbf{G})_{qk} (-\mathbf{R}_{kq} \mathbf{A}_q + \mathbf{A}_k)_{im} (\mathbf{A}_k)_{im} \\
 &\quad \left. + ((\mathbf{G})_{qk} - (\mathbf{G})_{kq}) (-\mathbf{R}_{kq} \mathbf{B}_q + \mathbf{A}_k)_{im} (\mathbf{A}_k)_{im} \right) = 0 \quad (24)
 \end{aligned}$$

$$\begin{aligned}
 &\gamma \sum_{p=1}^{k-1} ((\mathbf{G})_{kp} - (\mathbf{G})_{pk}) (\mathbf{R}_{pk}^T \mathbf{R}_{pk} \mathbf{B}_k - \mathbf{R}_{pk}^T \mathbf{A}_p)_{im} (\mathbf{B}_k)_{im} \\
 &\quad + (\Upsilon_k)_{im} (\mathbf{B}_k)_{im} + \sigma (\mathbf{B}_k - \mathbf{A}_k)_{im} (\mathbf{B}_k)_{im} = 0 \quad (25)
 \end{aligned}$$

$$\begin{aligned}
 &-(\mathbf{Y}_k^T \mathbf{A}_k)_{jm} (\mathbf{X}_k)_{jm} + (\mathbf{X}_k \mathbf{A}_k^T \mathbf{A}_k)_{jm} (\mathbf{X}_k)_{jm} \\
 &+ \alpha (\mathbf{X}_k^{-1/2})_{jm} (\mathbf{X}_k)_{jm} - (\Theta_k)_{jm} (\mathbf{X}_k)_{jm} \\
 &+ \beta \left(\sum_{p=1}^{k-1} (\mathbf{G})_{pk} (\mathbf{G})_{kp} (\mathbf{D}_{pk2} \mathbf{X}_k - \mathbf{W}_{pk}^T \mathbf{X}_p)_{jm} (\mathbf{X}_k)_{jm} + \sum_{q=k+1}^{K+1} \right. \\
 &\quad ((\mathbf{G})_{kq} (\mathbf{G})_{qk} (\mathbf{D}_{kq1} \mathbf{X}_k - \mathbf{W}_{kq} \mathbf{X}_q)_{jm} (\mathbf{X}_k)_{jm} + ((\mathbf{G})_{qk} \\
 &\quad \left. - (\mathbf{G})_{kq}) (\mathbf{D}_{kq1} \mathbf{X}_k - \mathbf{W}_{kq} \mathbf{Z}_q)_{jm} (\mathbf{X}_k)_{jm} \right) = 0 \quad (26)
 \end{aligned}$$

$$\begin{aligned}
 &\beta \sum_{p=1}^{k-1} ((\mathbf{G})_{kp} - (\mathbf{G})_{pk}) (\mathbf{D}_{pk2} \mathbf{Z}_k - \mathbf{W}_{pk}^T \mathbf{X}_p)_{jm} (\mathbf{Z}_k)_{jm} \\
 &\quad + (\Theta_k)_{jm} (\mathbf{Z}_k)_{jm} + \rho (\mathbf{Z}_k - \mathbf{X}_k)_{jm} (\mathbf{Z}_k)_{jm} = 0. \quad (27)
 \end{aligned}$$

These equations lead to the update rules (7)–(12).

REFERENCES

- [1] L. Guanter *et al.*, “The EnMAP spaceborne imaging spectroscopy mission for earth observation,” *Remote Sens.*, vol. 7, no. 7, pp. 8830–8857, 2015.
- [2] A. Iwasaki, N. Ohgi, J. Tanii, T. Kawashima, and H. Inada, “Hyperspectral imager suite (HISUI)-Japanese hyper-multi spectral radiometer,” in *Proc. Int. Geosci. Remote Sens. Symp. (IGARSS)*, Vancouver, Canada, Jul. 2011, pp. 1025–1028.
- [3] S. Pignatti *et al.*, “The PRISMA hyperspectral mission: Science activities and opportunities for agriculture and land monitoring,” in *Proc. Int. Geosci. Remote Sens. Symp. (IGARSS)*, Melbourne, Australia, Jul. 2013, pp. 4558–4561.
- [4] R. O. Green, G. Asner, S. Ungar, and R. Knox, “NASA mission to measure global plant physiology and functional types,” in *Proc. Aerosp. Conf.*, Big Sky, MT, USA, Mar. 2008, pp. 1–7.
- [5] S. Michel, P. Gamet, and M. J. Lefevre-Fonollosa, “HYPXIM—A hyperspectral satellite defined for science, security and defence users,” in *Proc. IEEE Workshop Hyperspectral Image Signal Process., Evol. Remote Sens. (WHISPERS)*, Lisbon, Portugal, Jun. 2011, pp. 1–4.
- [6] J. R. Irons, J. L. Dwyer, and J. A. Barsi, “The next Landsat satellite: The Landsat data continuity mission,” *Remote Sens. Environ.*, vol. 122, pp. 11–21, Sep. 2012.
- [7] M. Druscha *et al.*, “Sentinel-2: ESA’s optical high-resolution mission for GMES operational services,” *Remote Sens. Environ.*, vol. 120, pp. 25–36, May 2012.
- [8] M. Frank and M. Canty, “Unsupervised change detection for hyperspectral images,” in *Proc. AVIRIS Workshop*, 2003.
- [9] V. Ortiz-Rivera, M. Véllez-Reyes, and B. Roysam, “Change detection in hyperspectral imagery using temporal principal components,” *Proc. SPIE*, vol. 6233, p. 623312, May 2006.
- [10] A. A. Nielsen, “The regularized iteratively reweighted MAD method for change detection in multi- and hyperspectral data,” *IEEE Trans. Image Process.*, vol. 16, no. 2, pp. 463–478, Feb. 2007.
- [11] C. Wu, B. Du, and L. Zhang, “A subspace-based change detection method for hyperspectral images,” *IEEE J. Sel. Topics Appl. Earth Observ. Remote Sens.*, vol. 6, no. 2, pp. 815–830, Apr. 2013.
- [12] W. A. Malila, “Change vector analysis: An approach for detecting forest changes with Landsat,” in *Proc. 6th Annu. Symp. Mach. Process. Remote Sens. Data*, West Lafayette, IN, USA, 1980, pp. 326–336.
- [13] F. Bovolo, S. Marchesi, and L. Bruzzone, “A framework for automatic and unsupervised detection of multiple changes in multitemporal images,” *IEEE Trans. Geosci. Remote Sens.*, vol. 50, no. 6, pp. 2196–2212, May 2012.
- [14] S. Liu, L. Bruzzone, F. Bovolo, M. Zanetti, and P. Du, “Sequential spectral change vector analysis for iteratively discovering and detecting multiple changes in hyperspectral images,” *IEEE Trans. Geosci. Remote Sens.*, vol. 53, no. 8, pp. 4363–4378, Aug. 2015.
- [15] A. Schaum and A. Stocker, “Hyperspectral change detection and supervised matched filtering based on covariance equalization,” *Proc. SPIE*, vol. 5425, pp. 77–90, Aug. 2004.
- [16] J. Theiler, C. Scovel, B. Wohlberg, and B. R. Roy, “Elliptically contoured distributions for anomalous change detection in hyperspectral imagery,” *IEEE Geosci. Remote Sens. Lett.*, vol. 7, no. 2, pp. 271–275, Apr. 2010.
- [17] J. Meola, M. T. Eismann, R. L. Moses, and J. N. Ash, “Detecting changes in hyperspectral imagery using a model-based approach,” *IEEE Trans. Geosci. Remote Sens.*, vol. 49, no. 7, pp. 2647–2661, Jul. 2011.
- [18] G. Camps-Valls, L. Gomez-Chova, J. Munoz-Mari, J. L. Rojo-Alvarez, and M. Martinez-Ramon, “Kernel-based framework for multitemporal and multisource remote sensing data classification and change detection,” *IEEE Trans. Geosci. Remote Sens.*, vol. 46, no. 6, pp. 1822–1835, Jun. 2008.
- [19] D. Lu, M. Batistella, and E. Moran, “Multitemporal spectral mixture analysis for Amazonian land-cover change detection,” *Can. J. Remote Sens.*, vol. 30, no. 1, pp. 87–100, 2004.
- [20] D. B. Lobell and G. P. Asner, “Cropland distributions from temporal unmixing of MODIS data,” *Remote Sens. Environ.*, vol. 93, no. 3, pp. 412–422, Nov. 2004.
- [21] M. A. Goenaga, M. C. Torres-Madronero, M. Velez-Reyes, S. J. Van Bloem, and J. D. China, “Unmixing analysis of a time series of hyperion images over the Guánica dry forest in Puerto Rico,” *IEEE J. Sel. Topics Appl. Earth Observ. Remote Sens.*, vol. 6, no. 2, pp. 329–338, Apr. 2013.

- [22] B. Somers and G. P. Asner, "Multi-temporal hyperspectral mixture analysis and feature selection for invasive species mapping in rainforests," *Remote Sens. Environ.*, vol. 136, pp. 14–27, Sep. 2013.
- [23] P. Du, S. Liu, P. Liu, K. Tan, and L. Cheng, "Sub-pixel change detection for urban land-cover analysis via multi-temporal remote sensing images," *Geo-Spatial Inf. Sci.*, vol. 17, no. 1, pp. 26–38, 2014.
- [24] Q. Du, L. Wasson, and R. King, "Unsupervised linear unmixing for change detection in multitemporal airborne hyperspectral imagery," in *Proc. IEEE Int. Workshop MultiTemp*, May 2005, pp. 136–140.
- [25] A. Ertürk and A. Plaza, "Informative change detection by unmixing for hyperspectral images," *IEEE Geosci. Remote Sens. Lett.*, vol. 12, no. 6, pp. 1252–1256, Jun. 2015.
- [26] A. Ertürk, M.-D. Iordache, and A. Plaza, "Sparse unmixing-based change detection for multitemporal hyperspectral images," *IEEE J. Sel. Topics Appl. Earth Observ. Remote Sens.*, vol. 9, no. 2, pp. 708–719, Feb. 2016.
- [27] N. Yokoya and X. X. Zhu, "Graph regularized coupled spectral unmixing for change detection," in *Proc. WHISPERS*, Tokyo, Japan, Jun. 2015, pp. 1–4.
- [28] S. Liu, L. Bruzzone, F. Bovolo, and P. Du, "Unsupervised multi-temporal spectral unmixing for detecting multiple changes in hyperspectral images," *IEEE Trans. Geosci. Remote Sens.*, vol. 54, no. 5, pp. 2733–2748, May 2016.
- [29] S. Henrot, J. Chanussot, and C. Jutten, "Dynamical spectral unmixing of multitemporal hyperspectral images," *IEEE Trans. Image Process.*, vol. 25, no. 7, pp. 3219–3232, Jul. 2016.
- [30] A. Singh, "Review article digital change detection techniques using remotely-sensed data," *Int. J. Remote Sens.*, vol. 10, no. 6, pp. 989–1003, 1989.
- [31] C. Song, C. E. Woodcock, K. C. Seto, M. P. Lenney, and S. A. Macomber, "Classification and change detection using Landsat TM data: When and how to correct atmospheric effects?" *Remote Sens. Environ.*, vol. 75, no. 2, pp. 230–244, 2001.
- [32] P. Coppin, I. Jonckheere, K. Nackaerts, B. Muys, and E. Lambin, "Review article digital change detection methods in ecosystem monitoring: A review," *Int. J. Remote Sens.*, vol. 25, no. 9, pp. 1565–1596, 2004.
- [33] N. Keshava and J. F. Mustard, "Spectral unmixing," *IEEE Signal Process. Mag.*, vol. 19, no. 1, pp. 44–57, Jan. 2002.
- [34] J. M. Bioucas-Dias *et al.*, "Hyperspectral unmixing overview: Geometrical, statistical, and sparse regression-based approaches," *IEEE J. Sel. Topics Appl. Earth Observ. Remote Sens.*, vol. 5, no. 2, pp. 354–379, Apr. 2012.
- [35] D. C. Heinz and C.-I. Chang, "Fully constrained least squares linear spectral mixture analysis method for material quantification in hyperspectral imagery," *IEEE Trans. Geosci. Remote Sens.*, vol. 39, no. 3, pp. 529–545, Mar. 2001.
- [36] D. A. Roberts, M. Gardner, R. Church, S. Ustin, G. Scheer, and R. O. Green, "Mapping chaparral in the Santa Monica Mountains using multiple endmember spectral mixture models," *Remote Sens. Environ.*, vol. 65, no. 3, pp. 267–279, Sep. 1998.
- [37] M.-D. Iordache, J. Bioucas-Dias, and A. Plaza, "Sparse unmixing of hyperspectral data," *IEEE Trans. Geosci. Remote Sens.*, vol. 49, no. 6, pp. 2014–2039, Jun. 2011.
- [38] M. D. Iordache, "A sparse regression approach to hyperspectral unmixing," Ph.D. dissertation, Dept. School Elect. Comput. Eng., IST, Lisbon, Portugal, 2011.
- [39] Y. Zhong, R. Feng, and L. Zhang, "Non-local sparse unmixing for hyperspectral remote sensing imagery," *IEEE J. Sel. Topics Appl. Earth Observ. Remote Sens.*, vol. 7, no. 6, pp. 1889–1909, Jun. 2014.
- [40] R. Feng, Y. Zhong, and L. Zhang, "Adaptive non-local Euclidean median sparse unmixing for hyperspectral imagery," *ISPRS J. Photogram. Remote Sens.*, vol. 97, pp. 9–24, Nov. 2014.
- [41] J. Bieniarz, E. Aguilera, X. X. Zhu, R. Müller, and P. Reinartz, "Joint sparsity model for multilook hyperspectral image unmixing," *IEEE Geosci. Remote Sens. Lett.*, vol. 12, no. 4, pp. 696–700, Apr. 2015.
- [42] J. W. Boardman, "Geometric mixture analysis of imaging spectrometry data," in *Proc. Int. Geosci. Remote Sens. Symp. (IGARSS) Surface Atmos. Remote Sens. Technol., Data Anal. Interpretation.*, vol. 4. Pasadena, CA, USA, Aug. 1994, pp. 2369–2371.
- [43] M. E. Winter, "N-FINDR: An algorithm for fast autonomous spectral end-member determination in hyperspectral data," *Proc. SPIE*, vol. 3753, pp. 266–275, Oct. 1999.
- [44] J. M. P. Nascimento and J. M. Bioucas-Dias, "Vertex component analysis: A fast algorithm to unmix hyperspectral data," *IEEE Trans. Geosci. Remote Sens.*, vol. 43, no. 4, pp. 898–910, Apr. 2005.
- [45] J. Li and J. Bioucas-Dias, "Minimum volume simplex analysis: A fast algorithm to unmix hyperspectral data," in *Proc. IEEE Int. Conf. Geosci. Remote Sens. (IGARSS)*, vol. 3, Sep. 2008, pp. 250–253.
- [46] D. D. Lee and H. S. Seung, "Learning the parts of objects by non-negative matrix factorization," *Nature*, vol. 401, pp. 788–791, Oct. 1999.
- [47] D. Cai, X. He, J. Han, and T. S. Huang, "Graph regularized nonnegative matrix factorization for data representation," *IEEE Trans. Pattern Anal. Mach. Intell.*, vol. 33, no. 8, pp. 1548–1560, Aug. 2010.
- [48] L. Miao and H. Qi, "Endmember extraction from highly mixed data using minimum volume constrained nonnegative matrix factorization," *IEEE Trans. Geosci. Remote Sens.*, vol. 45, no. 3, pp. 765–777, Mar. 2007.
- [49] S. Jia and Y. Qian, "Constrained nonnegative matrix factorization for hyperspectral unmixing," *IEEE Trans. Geosci. Remote Sens.*, vol. 47, no. 1, pp. 161–173, Jan. 2009.
- [50] A. Huck, M. Guillaume, and J. Blanc-Talon, "Minimum dispersion constrained nonnegative matrix factorization to unmix hyperspectral data," *IEEE Trans. Geosci. Remote Sens.*, vol. 48, no. 6, pp. 2590–2602, Jun. 2010.
- [51] X. Liu, W. Xia, B. Wang, and L. Zhang, "An approach based on constrained nonnegative matrix factorization to unmix hyperspectral data," *IEEE Trans. Geosci. Remote Sens.*, vol. 49, no. 2, pp. 757–772, Feb. 2011.
- [52] Y. Qian, S. Jia, J. Zhou, and A. Robles-Kelly, "Hyperspectral unmixing via $L_{1/2}$ sparsity-constrained nonnegative matrix factorization," *IEEE Trans. Geosci. Remote Sens.*, vol. 49, no. 11, pp. 4282–4297, Nov. 2011.
- [53] X. Lu, H. Wu, Y. Yuan, P. Yan, and X. Li, "Manifold regularized sparse NMF for hyperspectral unmixing," *IEEE Trans. Geosci. Remote Sens.*, vol. 51, no. 5, pp. 2815–2826, May 2013.
- [54] N. Yokoya, T. Yairi, and A. Iwasaki, "Coupled nonnegative matrix factorization unmixing for hyperspectral and multispectral data fusion," *IEEE Trans. Geosci. Remote Sens.*, vol. 50, no. 2, pp. 528–537, Feb. 2012.
- [55] P. O. Hoyer, "Non-negative matrix factorization with sparseness constraints," *J. Mach. Learn. Res.*, vol. 5, pp. 1457–1469, Nov. 2004.
- [56] S. L. Waslander, G. Inalhan, and C. J. Tomlin, *Decentralized Optimization Via Nash Bargaining*. Norwell, MA, USA: Kluwer, 2004.
- [57] V. Caselles and M. J. L. García, "An alternative simple approach to estimate atmospheric correction in multitemporal studies," *Int. J. Remote Sens.*, vol. 10, no. 6, pp. 1127–1134, 1989.
- [58] F. G. Hall, D. E. Strelbel, J. E. Nickeson, and S. J. Goetz, "Radiometric rectification: Toward a common radiometric response among multiband, multisensor images," *Remote Sens. Environ.*, vol. 35, pp. 11–27, Oct. 1991.
- [59] N. Yokoya, N. Mayumi, and A. Iwasaki, "Cross-calibration for data fusion of EO-1/hyperion and Terra/ASTER," *IEEE J. Sel. Topics Appl. Earth Observ. Remote Sens.*, vol. 6, no. 2, pp. 419–426, Apr. 2013.
- [60] T. Wang, G. Yan, H. Ren, and X. Mu, "Improved methods for spectral calibration of on-orbit imaging spectrometers," *IEEE Trans. Geosci. Remote Sens.*, vol. 48, no. 11, pp. 3924–3931, Nov. 2010.
- [61] G. D. Finlayson, S. Hordley, and P. M. Hubel, "Recovering device sensitivities with quadratic programming," in *Proc. IST/SID 6th Color Imag. Conf. Color Sci., Syst., Appl.*, Nov. 1998, pp. 90–95.
- [62] J. Plaza, E. M. T. Hendrix, and I. García, G. Martín, A. Plaza, "On endmember identification in hyperspectral images without pure pixels: A comparison of algorithms," *J. Math. Imag. Vis.*, vol. 42, pp. 163–175, Sep. 2012.
- [63] D. P. Bertsekas, *Constrained Optimization and Lagrange Multiplier Methods* (Optimization and Neural Computation Series). Belmont, MA, USA: Athena Scientific, 1996.
- [64] S. Nagashima, T. Aoki, T. Higuchi, and K. Kobayashi, "A subpixel image matching technique using phase-only correlation," in *Proc. IEEE Int. Symp. Intell. Signal Process. Commun. Syst.*, Dec. 2006, pp. 701–704.
- [65] R. Richter and D. Schlöpfer, *Atmospheric/Topographic Correction for Satellite Imagery: Atcor 2/3 Users Guide*, Köln, Germany: German Aerospace Center (DLR), 2015.



Naoto Yokoya (S'10–M'13) received the M.Sc. and Ph.D. degrees in aerospace engineering from the University of Tokyo, Tokyo, Japan, in 2010 and 2013, respectively.

From 2012 to 2013, he was a Research Fellow with the Japan Society for the Promotion of Science, Tokyo. Since 2013, he has been an Assistant Professor with the University of Tokyo. Since 2015, he has been an Alexander von Humboldt Research Fellow with the German Aerospace Center, Oberpfaffenhofen, Germany, and the Technical University of Munich, Munich, Germany. His research interests include image analysis and data fusion in remote sensing.



Xiao Xiang Zhu (S'10–M'12–SM'14) received the bachelor's degree in space engineering from the National University of Defense Technology, Changsha, China, in 2006, and the M.Sc., Dr.-Ing., and "Habilitation" degrees in signal processing from the Technical University of Munich (TUM), Munich, Germany, in 2008, 2011, and 2013, respectively.

Since 2011, she has been a Scientist with the Remote Sensing Technology Institute, German Aerospace Center (DLR), Oberpfaffenhofen, Germany, where she is the Head of the Team Signal Analysis. Since 2013, she has also been a Helmholtz Young Investigator Group Leader with TUM, and appointed as a TUM Junior Fellow. In 2015, she joined Signal Processing in Earth Observation, TUM, as a Professor. She was a Guest Scientist or a Visiting Professor with the Italian National Research Council, Naples, Italy, Fudan University, Shanghai, China, University of Tokyo, Tokyo, Japan, and the University of California, Los Angeles, CA, USA, in 2009, 2014, 2015, and 2016, respectively. Her research interests include advanced InSAR techniques such as high-dimensional tomographic SAR imaging and SqueeSAR, computer vision in remote sensing including object reconstruction and multidimensional data visualization, big data analysis in remote sensing, and modern signal processing, including innovative algorithms such as sparse reconstruction, nonlocal means filter, robust estimation, and deep learning, with applications in the field of remote sensing such as multi/hyperspectral image analysis.

Dr. Zhu is an Associate Editor of the IEEE TRANSACTIONS ON GEOSCIENCE AND REMOTE SENSING.



Antonio Plaza (M'05–SM'07–F'15) received the M.Sc. and Ph.D. degrees in computer engineering from the University of Extremadura, Badajoz, Spain, in 1999 and 2002, respectively.

He is currently the Head of the Hyperspectral Computing Laboratory, Department of Technology of Computers and Communications, University of Extremadura. He has authored more than 500 publications, including 193 JCR journal papers (over 140 in IEEE journals), 23 book chapters, and 285 peer-reviewed conference proceeding papers.

His research interests include hyperspectral data processing and parallel computing of remote sensing data.

Dr. Plaza is a Fellow of the IEEE for contributions to hyperspectral data processing and parallel computing of earth observation data. He was a recipient of the Best Column Award of the IEEE SIGNAL PROCESSING MAGAZINE in 2015, the 2013 Best Paper Award of the JOURNAL OF SELECTED TOPICS IN APPLIED EARTH OBSERVATIONS AND REMOTE SENSING (JSTARS) journal, the most highly cited paper (2005–2010) in the *Journal of Parallel and Distributed Computing*, the Best Paper Awards at the IEEE International Conference on Space Technology, the IEEE Symposium on Signal Processing and Information Technology, the recognition of Best Reviewers for the IEEE GEOSCIENCE AND REMOTE SENSING LETTERS in 2009, and the IEEE TRANSACTIONS ON GEOSCIENCE AND REMOTE SENSING in 2010, for which he served as an Associate Editor in 2007–2012. He is also an Associate Editor of the IEEE ACCESS, and a Guest Editor of ten special issues on hyperspectral remote sensing for different journals. He was a member of the Editorial Board of the IEEE GEOSCIENCE AND REMOTE SENSING NEWSLETTER (2011–2012) and the IEEE GEOSCIENCE AND REMOTE SENSING MAGAZINE in 2013, and the Steering Committee of the IEEE JOURNAL OF SELECTED TOPICS IN APPLIED EARTH OBSERVATIONS AND REMOTE SENSING. He served as the Director of Education activities for the IEEE Geoscience and Remote Sensing Society (GRSS) in 2011–2012, and is currently serving as the President of the Spanish Chapter of the IEEE GRSS. He has reviewed more than 500 manuscripts for over 50 different journals. He is currently the Editor-in-Chief of the IEEE TRANSACTIONS ON GEOSCIENCE AND REMOTE SENSING.